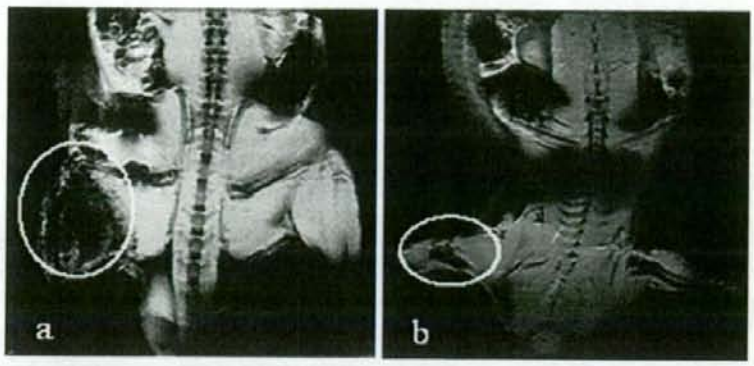

Figure 5. T2*-weighted MRI of right thigh after femoral injection of SPION-alginate with 0.5 h exposure time to magnetic field (A) or not (B). The images were taken at 10 h after injection, which still showed accumulation of iron oxide in target site with the magnetic field, since the strong signal intensity decreased (white circle in A). But the iron oxide did not accumulate in target site (white circle in B), which could be attributed to the slight change of signal intensity without the magnetic field.

upon exposure to various concentrations of SPION-alginate for 24 h with or without NCS (Fig. 6).

Cell labeling with SPION-alginate

Following 1–24 h incubation with SPION-alginate, almost all RAW264.7 cell labeling were achieved. It was evident that the labeled RAW264.7 cells contained abundant Fe_3O_4 nanoparticles in the cytoplasm after incubation with the iron concentration of 12.5, 25.0, and 50.0 μg/mL. The SPION-alginate was internalized into RAW264.7 cells in a concentration- and time- dependent manner (Fig. 7). At a concentration of 25.0 μg/mL, cells started to internalize iron particles already after 1 h incubation [Fig. 7(B)] and the internalization was increased from 1 to 24 h incubation [Fig. 7(C–E)]. For 5 h of incubation at different concentrations, it showed the amount of Prussian blue positive particles in cytoplasma as follow: 50.0 > 25.0 > 12.5 μg/mL. However, no stainable iron was detected in the control cells [Fig. 7(A)].

TABLE I
Hemolysis Percentage of Rabbit Erythrocytes at 37°C After 3 h Incubation With Different Concentrations of SPION-Alginate

SPION-Alginate Concentration (mg Fe/mL)		
Bulk Suspension	Final Suspension	Hemolysis (%)
2.08	0.04	−0.34 ± 0.16
2.08	0.08	0.71 ± 0.78
2.08	0.12	0.29 ± 0.16
2.08	0.17	1.15 ± 0.34
2.08	0.21	2.08 ± 1.48
3.62	0.07	0.23 ± 1.15
3.62	0.14	0.62 ± 1.41
3.62	0.22	1.03 ± 0.70
3.62	0.29	3.19 ± 1.56
3.62	0.36	3.19 ± 1.09
5.74	0.11	1.38 ± 0.96
5.74	0.23	0.62 ± 0.53
5.74	0.34	2.21 ± 0.89
5.74	0.46	2.35 ± 1.74
5.74	0.57	3.24 ± 0.26

Data represent mean ± SD (n = 3). The hemolysis >5% was regarded as erythrocytes hemolysis.

DISCUSSION

To optimize magnetic targeting, several factors need to be considered, (a) the magnetic field, including magnetic intensity and magnetic intensity gradient, should be of sufficient strength to attract the magnetic nanoparticles into the target site; (b) the

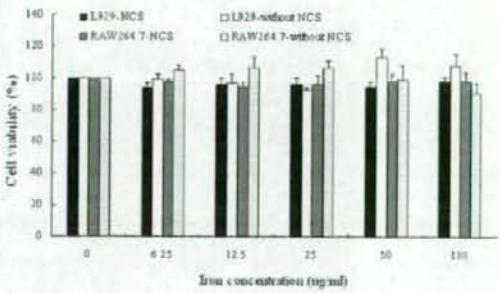

Figure 6. Viability of L929 cells and RAW264.7 cells exposed to SPION-alginate for 24 h at various iron concentrations ranging from 6.125 to 100.0 μg/mL. Cell viability is expressed as the mean ± SD of the percentage of absorbance of controls, where 100% equals viability of the control cells. The experiments were performed in hexakis and were repeated three times.

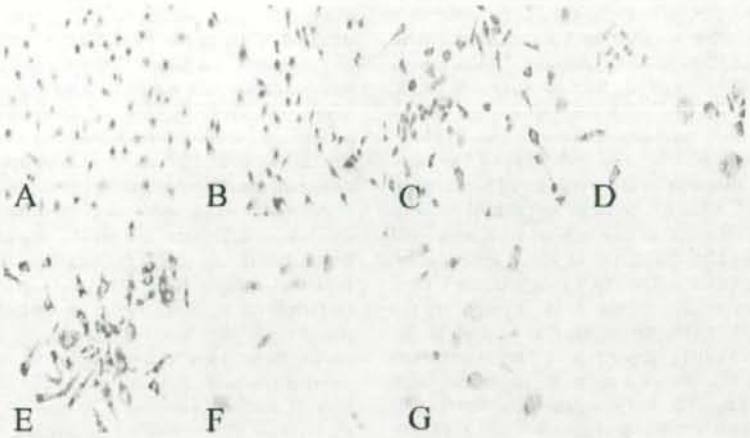

Figure 7. Photomicrographs of Prussian blue stained labeled and control RAW264.7 cells. Cells were cultured with different concentrations of SPION-alginate and harvested after different incubation times. Note the abundant iron particles in the cytoplasm of the cells (blue dots). (A) control; (B) SPION-alginate 25.0 μg/mL, 1 h; (C) SPION-alginate 25.0 μg/mL, 5 h; (D) SPION-alginate 25.0 μg/mL, 12 h; (E) SPION-alginte 25.0 μg/mL, 24 h; (F) SPION-alginate 12.5 μg/mL, 5 h; (G) SPION-alginate 50.0 μg/mL, 5 h (×400 magnification). [Color figure can be viewed in the online issue, which is available at www.interscience.wiley.com.]

magnetic particles should be of a suitable size with good magnetization and biocompatibility; (c) the method of injection should have good access to the target site and the particles should avoid clearance by RES.

In the magnetic targeting study, we employed three methods: iron content measurement, histological evaluation, and MRI. The SPION-alginate could be retained in the target site under the magnetic field with the localization ratio of 56% *in vitro* and the localization ratio of 20% *in vivo*, while reducing accumulation in the liver and spleen (Fig. 2). In addition, without magnetic field, the SPION-alginate would not be retained at the injection site (Fig. 4). The localization ratio of SPION-alginate *in vivo* was lower than that *in vitro* under the same magnetic field. One of the most important factors affecting the localization ratio of SPION-alginate *in vivo* was the rapid blood flow rate approximately 30 cm/s in large arteries.[20] Hence, part of the SPION-alginate would be flushed by the high blood flow rate which caused the decrease of the localization ratio *in vivo*. In addition, the SPION-alginate was still be phagocytosed by RES although by the artery administration.

Without magnetic field, the accumulation of SPION-alginate in liver (47.54%) and in spleen (6.66%) by femoral artery administration at 0.5 h was significantly lower than that in liver (>80%) and in spleen (10%) by vein administration at 0.5 h (data were not shown), which proved that artery injection was more advantageous than vein injection when the SPION-alginate was targeted to the sites other than liver and spleen. Furthermore, it was reported that intravenous infusion of magnetic drug particles was ineffective to make tumor remission, but the combination of artery infusion with a magnetic field was safe and effective.[2] At present, intraarterial injection of chemotherapeutic agents is approved and well accepted for treatment of liver metastases, and it has occasionally been used for other tumor types such as inoperable head and neck tumors.[21] Many other studies also confirmed the efficacy of arterial administration of magnetic targeting.[3,4,22,23] Currently, the doxorubicin hydrochloride absorbed to magnetic targeted carriers (MTC-DOX) is under clinical investigation for the treatment of patients with primary hepatocellular carcinoma (HCC). It was reported that the particles could be retained at HCC under the applied magnetic field after 28 days by intraarterial administration in human clinical trials.[21] Furthermore, a multicenter, phase I/II trial of hepatic intraarterial deliver of MTC-DOX in patients with HCC and a phase I/II dose escalation study of MTC-DOX in patients with metastatic liver tumors have been undertaken, the results indicated that MTC-DOX could be localized regionally following intraarterial administration without clinically significant toxicities in all cases.[4,23]

The magnetization of the particles was related to the magnetic field strength and the magnetic field gradient. The higher magnetic flux density and magnetic gradient it is, the better the location effect is.[2] Until now, the maximum magnetic field reported was a magnetic flux density of a maximum of 1.7

and 1.0 T at 10 mm below the tip of the pole shoe produced by electric magnet[2] and a remanence field of 1.3 T by NdFeB-permanent magnet.[24] In previous studies, it was suggested that a magnetic field strength of 0.8 T was sufficient to exceed linear blood flow in the intratumoral vasculature.[20] However, a magnetic field of only 250–1000 G has been used to locate the iron oxide particles (0.5–5 μm) in liver and lung.[25] One of the most important reasons for the great difference in strength of magnetic field used above was the difference of the magnetization of iron oxide particles. The high magnetic flux density focused onto the target area is one of the obstacles for effectively targeting. The use of larger particles, as previously suggested by Lübbe and Bergemann,[26] and the use of a stronger magnetic field, are the two approaches to overcome this problem. If the magnetization of the particle is low, a higher magnetic field is needed and vice versa. Therefore, the selection of magnetic field depends on the magnetization of the magnetic carrier. NdFeB-permanent magnet with the surface magnetic field of 3500 G and with the magnetic gradient of 2000 G/cm was used in this study. We achieved a high concentration of iron oxide within the target site after femoral artery administration of the SPION-alginate, which was seen by quantitative evaluation of iron (Figs. 2 and 3), histological (Fig. 4) and MRI (Fig. 5) methods.

As respect to the time of magnetic field added, the shortest time reported was 15 min and the longest time was 24 h.[22,24] In this study, the SPION-alginate had some magnetic targeting effect under the magnetic field at 0.5 h and as the time was prolonged to 2 h, it did not produce better magnetic target. It might be explained that the iron oxide of strong magnetism would soon be absorbed under the magnetic field of 3500 G, while those of poor magnetism would not be absorbed as the time increased and could still be phagocytosed by RES. We speculate that the time of magnetic field added depends both on the magnetization of the particles and the intensity of magnetic field. The higher magnetization of particles and the higher intensity of magnetic field, the shorter time of magnetic field.

Concerning magnetic targeting, there are many practical applications of the magnetic nanoparticles, such as magnetic drug targeting,[2–5,20,23,24] magnetic fluid hyperthermia,[6] and MRI.[9,19] The magnetic nanoparticles can act as carriers of drug and gene for site-specific drug and gene delivery. For example, the SPION-alginate can be functionalized with specific drug like chemotherapeutic drugs for chemical therapy or radioactive isotope for radionuclide therapy. Another promising application of the magnetic nanoparticles is magnetic fluid hyperthermia as one of cancer therapy strategies. When the magnetic carrier is localized at the target site with the applied magnetic field, some heat is generated under an alternating magnetic field due to magnetic hysteresis of magnetic particles. Furthermore, the magnetic nanoparticles can result in a strong decrease in MR signal intensity (negative enhancement) of the tissues where they accumulate. Therefore, it will play an important role in MR contrast imaging to better discriminate healthy and pathological tissues.

Although some encouraging data were achieved in this study, there are many issues to be further investigated on magnetic targeting. For example, a potential complication that could arise with the use of ferrofluid is the fact that an embolization process could occur after magnetic targeting, and the embolization is to some extent favorable for cancer treatment because of their cut-off of the blood and nutrition of tumor.[8] However, it was reported that the therapeutic effect resulted from the action of the chemotherapeutic agent itself, rather than intratumoral embolization by the particles.[2] On the other hand, the localization accuracy of the particles at the target site needs to be optimized, and the design of the magnetic field with greater magnetic field intensity and magnetic field gradient is quite important and needs to be improved.

Compared with the corresponding control cells, no significant change was observed in the viability of RAW264.7 cells and L929 cells with various different concentrations of SPION-alginate for 24 h incubation with or without serum (Fig. 6). Hence, we considered that the SPION-alginate was not toxic to RAW264.7 cells and L929 cells. In addition, the SPION-alginate did not induce erythrocytes hemolysis and erythrocytes aggregation. Accordingly, the SPION-alginate was generally considered to be of good biocompatibility.

Figure 7 showed that the labeled RAW264.7 cells contained abundant Fe_3O_4 nanoparticles in the cytoplasm after 1–24 h incubation with the various concentrations of SPION-alginate. The high RAW264.7 labeling efficiency with the SPION-alginate seems to be related firstly to the nonspecific process of nanoparticles adsorption on the cell membrane in the form of clusters, secondly to their subsequent internalization into endosomes, as introduced by other authors.[14,27] The interaction of the SPION-alginate with living cells should be further investigated. Moreover, the Fe_3O_4 nanoparticles bound to alginate macromolecule strands like "fruit" in the "tree," not simply coated by the polymer. They were visually confirmed by atomic force microscopy.[10] It is indicated that alginate would not hamper their interactions with cell membrane, which could be caused by steric coating effect. Besides, the good bioadhesion property of alginate is beneficial to the adsorption of SPION-alginate on the cell membrane. Because of the nonspecific cellular uptake mediated by adsorptive

endocytosis, the SPION-alginate labeling may be nonspecific and potentially applicable to a wide variety of cells, making it useful for cellular imaging strategies.

CONCLUSIONS

With magnetic field, the SPION-alginate had a localization ratio of 56% *in vitro* and 20% *in vivo*, meanwhile, the contents of the SPION-alginate in liver and spleen were reduced. The magnetic targeting effect was established by evaluating the iron content ratio of target site/nontarget site, and was visually confirmed by histological evaluation and MRI. Furthermore, the SPION-alginate was considered to be biocompatible in respects of cytotoxicity and hemolysis.

References

1. Häfeli UO. Magnetically modulated therapeutic systems. Int J Pharm 2004;277:19–24.
2. Alexiou C, Arnold W, Klein RJ, Parak FG, Hulin P, Bergemann C, Erhardt W, Wagenpfeil S, Lübbe AS. Locoregional cancer treatment with magnetic drug targeting. Cancer Res 2000;60:6641–6648.
3. Leakakos T, Ji C, Lawson G, Peterson C, Goodwin S. Intravesical administration of doxorubicin to swine bladder using magnetically targeted carriers. Cancer Chemother Pharmacol 2003;51:445–450.
4. Just R, Hoh C, Vogl T, Neese P, Doemeny J, Schechter M, Varney R, Stanton W, Schiemann M, Goldfarb P. A phase I/II single arm trial to determine the safety, tolerability, and biological activity of intrahepatic delivery of doxorubicin hydrochloride adsorbed to magnetic targeted carriers (MTX-DOX) in patients with metastatic tumors in the liver. Eur J Cancer Suppl 2003;1:S292–S293.
5. Häfeli U, Pauer G, Failing S, Tapolsky G. Radiolabeling of magnetic particles with rhenium-188 for cancer therapy. J Magn Magn Mater 2001;225:73–78.
6. Jordan A, Scholz R, Maier-Hauff K, Johannsen M, Wust P, Nadobny J, Schirra H, Schmidt H, Deger S, Loening S, Lanksch W, Felix R. Presentation of a new magnetic field therapy system for the treatment of human solid tumors with magnetic fluid hyperthermia. J Magn Magn Mater 2001;225:118–126.
7. Scherer F, Anton M, Schillinger U, Henke J, Bergemann C, Krüger A, Gänsbacher B, Plank C. Magnetofection: Enhancing and targeting gene delivery by magnetic force in vitro and in vivo. Gene Ther 2002;9:102–109.
8. Widder KJ, Senyei AE, Scarpelli GD. Magnetic microspheres: A model system for site specific drug delivery in vivo. Proc Soc Exp Biol Med 1978;158:141–146.
9. Wang YX, Hussain SM, Krestin GP. Superparamagnetic iron oxide contrast agents: Physicochemical characteristics and applications in MR imaging. Eur Radiol 2001;11:2319–2331.
10. Ma HL, Qi XR, Maitani Y, Nagai T. Preparation and characterization of superparamagnetic iron oxide nanoparticles stabilized by alginate. Int J Pharm 2007;333:177–186.
11. Sgouras D, Duncan R. Methods for the evaluation of biocompatibility of soluble synthetic polymers which have potential for biomedical use: 1-Use of the tetrazolium-based colorimetric assay (MTT) as a preliminary screen for evaluation of in vitro cytotoxicity. J Mater Sci: Mater Med 1990;1:61–68.
12. Biological Evaluation for Medical Devices, Part 5: Tests for Cytotoxicity: In Vitro Methods. United States Pharmacopeia XXIII, 1995.
13. Biological Evaluation of Medical Devices, Part 5: Test for In Vitro Cytotoxicity. ISO 10993-5 (EN 30993-5), 1999.
14. Wilhelm C, Billotey C, Roger J, Pons JN, Bacri JC, Gazeau F. Intracellular uptake of anionic superparamagnetic nanoparticles as a function of their surface coating. Biomaterials 2003;24:1001–1011.
15. Hagar W, Vichinsky EP, Theil EC. Liver ferritin subunit ratios in neonatal hemochromatosis. Pediatr Hematol Oncol 2003;20:229–235.
16. Regulations of new drug license application in China.State Food and Drug Administration in China; 1999. p 24.
17. Mosmann T. Rapid colorimetric assay for cellular growth and survival: Application to proliferation and cytotoxicity assays. J Immunol Methods 1983;65:55–63.
18. Arbab AS, Bashaw LA, Miller BR, Jordan EK, Lewis BK, Kalish H, Frank JA. Characterization of biophysical and metabolic properties of cells labeled with superparamagnetic iron oxide nanoparticles and transfection agent for cellular MR imaging. Radiology 2003;229:838–846.
19. Saini S, Stark DD, Hahn PF, Wittenberg J, Brady TJ, Ferrucci JT. Ferrite particles: A superparamagnetic MR contrast agent for the reticuloendothelial system. Radiology 1987;162:211–216.
20. Senyei A, Widder K, Czerlinski C. Magnetic guidance of drug carrying microspheres. J Appl Phys 1978;49:3578–3583.
21. Link KH, Kornmann M, Formenti A, Leder G, Sunelaitis E, Schatz M, Pressmar J, Beger HG. Regional chemotherapy of non-resectable liver metastases from colorectal cancer-literature and institutional review. Langenbecks Arch Surg 1999;384:344–353.
22. Rudge S, Peterson C, Vessely C, Koda J, Stevens S, Catterall L. Adsorption and desorption of chemotherapeutic drugs from a magnetically targeted carrier (MTC). J Control Release 2001;74:335–340.
23. Koda J, Venook A, Walser E, Goodwin S. A multicenter, phase I/II trial of hepatic intra-arterial delivery of doxorubicin hydrochloride adsorbed to magnetic targeted carriers in patients with hepatocellular carcinoma. Eur J Cancer 2002;38(Suppl 7):S18.
24. Schulze K, Koch A, Schöpf B, Petri A, Steitz B, Chastellain M, Hofmann M, Hofmann H, von Rechenberg B. Intraarticular application of superparamagnetic nanoparticles and their uptake by synovial membrane—An experimental study in sheep. J Magn Mag Mater 2005;293:419–432.
25. Goodwin S, Peterson C, Hoh C, Bittner C. Targeting and retention of magnetic targeted carriers (MTCs) enhancing intra-arterial chemotherapy. J Magn Mag Mater 1999;194:132–139.
26. Lübbe AS, Bergemann C.Selected preclinical and first clinical experiences with magnetically targeted 4'-epidoxorubicin in patients with advanced solid tumors. In: Häfeli U, Schütt W, Teller J, Zborowski M, editors. Scientific and Clinical Application of Magnetic Carriers. New York:Plenum; 1997. p 457–480.
27. Wilhelm C, Gazeau F, Roger J, Pons JN, Bacri JC. Interaction of anionic superparamagnetic nanoparticles with cells: Kinetic analyses of membrane adsorption and subsequent internalization. Langmuir 2002;18:8148–8155.

Available online at www.sciencedirect.com
ScienceDirect
International Journal of Pharmaceutics 354 (2008) 217–226
INTERNATIONAL JOURNAL OF PHARMACEUTICS
www.elsevier.com/locate/ijpharm

Pharmaceutical Nanotechnology

Superparamagnetic iron oxide nanoparticles stabilized by alginate: Pharmacokinetics, tissue distribution, and applications in detecting liver cancers

Hui Li Ma [a], Yu Feng Xu [b], Xian Rong Qi [a,*], Yoshie Maitani [c], Tsuneji Nagai [d]

[a] Department of Pharmaceutics, School of Pharmaceutical Sciences, Peking University, Beijing 100083, China
[b] Department of Radiology, First Hospital, Peking University, Beijing 100034, China
[c] Institute of Medicinal Chemistry, Hoshi University, Shinagawa-Ku, Tokyo 142-8501, Japan
[d] The Nagai Foundation Tokyo, Hon-Komagome, Bunkyo-ku, Tokyo 113-0021, Japan

Received 13 August 2007; received in revised form 18 November 2007; accepted 20 November 2007
Available online 28 November 2007

Abstract

The objectives of this study were to describe the pharmacokinetics and tissue distribution of superparamagnetic iron oxide nanoparticle (SPIO) stabilized with alginate (SPIO-alginate), and investigate its potential in detecting liver cancers as a newly developed magnetic resonance (MR) contrast agent. Pharmacokinetics and tissue distribution of SPIO-alginate were investigated in Sprague–Dawley rats. The results showed that SPIO-alginate was eliminated rapidly from serum with the half-life of 0.27 h at 109.5 μmol Fe/kg and accumulated dominantly in liver and spleen with a total percentage of more than 90% of dose after intravenous injection. The studies of pharmacokinetics and distribution of SPIO-alginate in rats indicated the MR contrast agent, based on SPIO, mainly accumulating in targeting organs that contain phagocytosing cells, i.e. liver and spleen. The efficacies in detecting hepatocellular carcinoma (HCC) of rat with primary liver cancer and xenograft liver cancers of rabbit were investigated before and after injection of SPIO-alginate. The signal intensity of liver parenchyma in rabbit with VX2 tumor after injection of SPIO-alginate was reduced sharply resulting in a significant contrast between liver parenchyma and tumor. Detection of the HCC in rat model was also demonstrated. The present study provides evidence that SPIO-alginate might have the ability to improve the detection of liver tumors as an MR contrast agent, and the efficacy is associated with the SPIO specifically located in Kupffer cells in hepatic sinusoid.

Keywords: Superparamagnetic iron oxide nanoparticles (SPIO); Pharmacokinetics; Distribution; Liver cancers; Contrast agent; Alginate

1. Introduction

MR imaging is one of the most useful non-invasive methods in the field of diagnostic imaging, which is characterized by its high resolution of soft-tissues and by its non-exposure to radiation. To better differentiate healthy and pathological tissues, paramagnetic gadolinium based contrast agents which shorten the longitudinal relaxation time (T1) and increase the contrast of the image (positive enhancement) are mainly used today (Weinmann et al., 2003). Compared to gadolinium based contrast agents, SPIO can produce enhanced relaxation rates in specific organs at lower dose than paramagnetic ions, because of their larger magnetic moment (Corot et al., 2006; Wang et al., 2001). Generally speaking, the transverse relaxation (T2 and T2*) effect of SPIO is mostly utilized in detection of liver lesions by MR imaging. SPIO are distributed in reticuloendothelial cells, such as Kupffer cells (KCs), according to phagocytic activity, and cause local field inhomogeneities that produce rapid dephasing of neighboring proton spins, resulting in a shortening of T2 relaxation times. In contrast, liver tumors such as metastatic liver cancer and HCC cannot absorb these agents because of the lack of reticuloendothelial cells. Therefore, the contrast between tumor tissue and surrounding normal liver tissue is enhanced because of signal loss in the liver tissue (Saini et al., 1987). Hence, SPIO can produce a strong decrease in MR signal intensity (negative enhancement) in the tissues where they accumulate, such as the liver, spleen, bone marrow, and lymph node (Saini et al., 1987; Corot et al., 2006).

* Corresponding author. Tel.: +86 10 82801584; fax: +86 10 82802791.
E-mail address: qixr2001@yahoo.com.cn (X.R. Qi).

0378-5173/$ – see front matter © 2007 Elsevier B.V. All rights reserved.
doi:10.1016/j.ijpharm.2007.11.036

Until now, two SPIO preparations have already been approved for clinical use, especially for liver MR imaging, such as Ferumoxides (i.e. Endorem® in Europe, Feridex® in the USA and Japan, Advanced Magnetics, USA) coated with dextran (Weissleder et al., 1989), and Ferucarbutran (i.e. Resovist® in Europe and Japan, Schering, Germany) coated with carboxydextran (Reimer et al., 1995). Furthermore, several SPIO preparations have been investigated in human for imaging applications, such as VSOP-C184, a very small SPIO coated with citrate (Taupitz et al., 2004), and Feruglose (Clariscan; Amersham Health, Oslo, Norway) where iron oxide particles have been stabilized with oxidized starch that consist of carbohydrate-polyethylene glycol (Kellar et al., 2000).

In our previous work, SPIO stabilized with alginate (SPIO-alginate) have been successfully prepared (Ma et al., 2007) and the SPIO-alginate have good biocompatibility and some magnetic targeting under the magnetic field (Ma et al., 2007a). As the coating material of iron oxide, alginate is known for binding many multivalent ions *in vitro* such as Ca^{2+}, Ba^{2+}, Fe^{2+}, and Fe^{3+}. The high stability of SPIO-alginate is probably caused by the binding of the carboxyl group of alginate to iron oxide nuclei (Ma et al., 2007). It was reported that the absorption of Fe, Cr, and Co was significantly reduced after oral administration of sodium alginate in rats, while Ca and Zn absorption was not affected (Harmut-Hoene and Schelenz, 1980). Hence, it is necessary to investigate the effect of alginate and SPIO-alginate on the iron level *in vivo*, even if some COO^- terminals of alginate have been bound to iron oxide in SPIO-alginate.

We presumed that using SPIO-alginate as an intravenous contrast medium, detection of malignant liver lesions by MR imaging might be improved. Once iron oxide particles are taken up by the macrophages situated in the liver of reticuloendothelial system (RES) but not by tumor cells, the contrast between liver parenchyma and liver lesion would significantly increase, which is caused by the distinct signal loss in liver parenchyma and the almost stable signal intensity in malignant liver tumors (Saini et al., 1987; Clement et al., 1991; Nakayama et al., 1998; Imai et al., 2000; Bourrinet et al., 2006).

To investigate whether this highly stabilized SPIO-alginate is a kind of ideal MR contrast for liver imaging, the pharmacokinetics and tissue distribution of SPIO-alginate in rats were first examined in this study. After that, the efficacy of SPIO-alginate for the detection of liver cancers was evaluated in two kinds of tumor models, VX2 liver tumor in rabbit and primary liver cancer in rat.

2. Materials and methods

2.1. Contrast agent

Typical iron oxide nanoparticles were Fe_3O_4 with a core diameter of 5–10 nm. Meanwhile, SPIO-alginate had a hydrodynamic diameter of 193.8 nm with good stability as well as superparamagnetism, and its ξ-potential was −65.0 mV. T1 and T2 relaxivities of SPIO-alginate in physiological saline (1.5 T, 20 °C) were 7.86 ± 0.20 and $281.2 \pm 26.4\ s^{-1}\ mM^{-1}$, respectively. Other properties of SPIO-alginate were described in detail in the previous publication (Ma et al., 2007, 2007a). For MR imaging experiment, SPIO-alginate was diluted to a concentration of 8.9 μmol Fe/mL with physiological saline.

2.2. Pharmacokinetics, tissue distribution and histological evaluation in normal rats

Male Sprague–Dawley rats weighing 150 ± 20 g were purchased from Experimental Animal Center of Peking University, China. All care and handling of animals were performed with the approval of Institutional Authority for Laboratory Animal Care of Peking University, which followed the guidelines established by the China Council for Animal Care. The animals were anesthetized by intraperitoneal injection of 1.0 g/kg of ethyl carbamate. The pharmacokinetics studies (using whole blood) were carried out with 29 rats which were divided into four groups randomly. The rats were intravenously injected with the following formulations individually: SPIO-alginate at a dose of 109.5 μmol Fe/kg (SPIO-low dose) ($n = 18$), SPIO-alginate at a dose of 218.9 μmol Fe/kg (SPIO-high dose) ($n = 3$), 1 mL 0.6% (w/v) alginate solution (alginate solution) ($n = 3$), and 1 mL physiological saline (saline) ($n = 5$). About 0.3 mL blood samples were taken by retro-orbital venous plexus puncture at 0 min (before intravenous injection), 5 min, 10 min, 30 min, 1 h, 3 h, 6 h, 12 h, 24 h, 48 h, 96 h, 168 h, and 336 h after injection, respectively.

The pharmacokinetics studies (using serum) were obtained in rats by quantitative determination of iron in serum. Twenty rats were divided into four groups ($n = 5$ per group) in random and injected with SPIO-low dose, SPIO-high dose, alginate solution, and saline, respectively. About 0.6 mL blood samples were collected from retro-orbital venous plexus puncture at 0 min, 5 min, 10 min, 30 min, 1 h, 3 h, 6 h, 12 h, and 24 h after injection, respectively. Then each clotted blood sample was centrifuged at 7000 rpm for 20 min to get serum sample.

The basic serum iron concentration was calculated from the average serum iron concentration at 0 min of all the rats. The serum iron concentrations at various time points after administration were calculated by subtracting the basic serum iron concentration. Serum iron concentration–time profiles were analyzed by WinNonlin computer software, Version 3.1 (Pharsight Corporation, Mountain View, CA), using noncompartmental method with bolus intravenously administration. The following parameters were obtained: maximum tissue concentration (C_{max}), elimination rate constant (λ), elimination half-life ($T_{1/2}$), area under the curve (AUC), and mean residence time (MRT).

The tissue distribution of SPIO-alginate at a dose of 109.5 μmol Fe/kg in rats (total 21) were studied at 0, 0.5, 3, 24, 48, 96, and 336 h after injection, which was performed simultaneously with the blood pharmacokinetics study of SPIO-low dose. Tissues of interest (blood, liver, spleen, heart, lungs, and kidneys) were collected immediately at various time points, weighted, and frozen at −20 °C until analysis.

Liver and spleen concentration-time profiles were analyzed by WinNonlin computer software using a noncompartmental method with a single extravascular dosing. The iron concentrations in liver and spleen at various time points were calculated

by subtracting the iron concentration in liver or in spleen at 0 h (before injection), respectively. The following parameters were obtained: time of maximum concentration (T_{max}), C_{max}, λ, $T_{1/2}$, AUC, and MRT.

Liver and spleen were removed at 0.5, 24, 96, and 336 h after injection of SPIO-low dose, and at 336 h after injection of SPIO-high dose and alginate solution, respectively. Then the samples were fixed in 4% paraformaldehyde solution (pH 7.4) for hematoxylin-eosin (HE) staining and Perls staining. The liver and spleen section specimens were examined under a light microscopy after staining.

2.3. Iron content measurement

For quantitative determination of iron content, blood, serum and tissue samples were digested in a beaker with the mixed acid of HNO_3–$HClO_4$ (4:1, v:v) for 48 h at room temperature, and then evaporated to dryness at 100 °C by sand bath with electric hot plate. Finally 37.5% HCl solution was added to the beaker to dissolve the solid and the iron content was determined by *o*-phenanthroline method (Hagar et al., 2003).

2.4. Tumor models of rats and rabbits

Male Sprague–Dawley rats (130–140 g, total 35) were used. The model of primary liver cancer in rats ($n = 29$) was established by giving 70 mg diethylnitrosoamine (DENA, Sigma–Aldrich, USA) per kg weight 14 times at 7-d intervals through intragastric administration with physiological saline. As DENA was sensitive to light, a fresh solution was prepared for each administration and kept in dark bottles for short periods. The rats of control group ($n = 6$) were raised in the normal condition.

VX2 rabbit tumor was cut into small pieces (about 1 mm^3), and then implanted into left hepatic lobe to establish single liver cancer in rabbit. After implantation, VX2 tumor rapidly developed in the liver and the implanted tumor formation was detected by computed tomography (CT) on week 2. The surgery and implantation procedures have been described in detail in the previous publication (Hauff et al., 1997).

2.5. MR imaging in normal rat

All MR imaging examinations were performed by using a clinical 3.0 T MR scanner (Signa Horizon, General Electric Medical Systems, Milwaukee, WI) with a surface coil. For the investigations of liver enhancement in normal rats, the normal rats ($n = 6$) were imaged before and after injection of SPIO-alginate at a dose of 20 μmol Fe/kg through femoral vein. T1-weighted fast spin echo (FSE) or spoiled gradient-recalled (SPGR) sequence, T2-weighted fast recovery fast spin echo (FRFSE) sequence, and T2*-weighted gradient-recalled echo (GRE) sequence were used for the MR imaging. All the sequences were applied with a bandwidth of 31.25 kHz and slice thickness of 3 mm. Other parameters were as follows: T1-weighted FSE sequence (TE 14.6 ms; TR 800 ms; Echo train length 3; Matrix 288 × 192; NEX 4; FOV 8 × 8); T1-weighted SPGR sequence (TE 3.7 ms; TR 100 ms; Flip angles 60°; Matrix 128 × 128; NEX 6; FOV 8 × 4); T2-weighted FRFSE sequence (TE 150 ms; TR 3000 ms; Echo train length 21; Matrix 128 × 128; NEX 6; FOV 8 × 5.6); T2*-weighted GRE sequence (TE 4.7 ms; TR 300 ms; Flip angles 15°; Matrix 128 × 128; NEX 6; FOV 8 × 4).

2.6. MR imaging in tumor animals and histological evaluation

For rabbits with VX2 tumor, unenhanced and enhanced T2*-weighted images were investigated before and after injection of SPIO-alginate at a dose of 20 μmol Fe/kg using SPGR sequence with the following parameters: TR of 220 ms, TE of 5.2 ms, flip angles of 70°, slice thickness of 4 mm, slice gap of 1.0 mm, matrix of 512 × 160, field of view of 13 × 13, and bandwidth of 62.5 kHz.

For rats with primary liver cancer, unenhanced and enhanced images were obtained before and after injection of SPIO-alginate at a dose of 20 μmol Fe/kg using T2*-weighted GRE sequence with the parameters just mentioned above in MR imaging for normal rats. The rats were sacrificed within 2–12 h after MR imaging evaluation. Then, liver specimens were fixed, the size, number, and shape of the lesions were observed, and the lesions were histologically identified after HE staining and Perls staining. The pathological changes e.g. hyperplastic nodules, cirrhotic and HCC, were also observed.

2.7. Imaging analysis

Quantitative analysis was performed by using an operator defined region of interest (ROI) of 6 mm^2 on T1-weighted, T2-weighted and T2*-weighted images, respectively. Major vessels were avoided when the signal intensities of liver parenchyma and tumor were measured. Measurements included signal intensity (SI) of the HCC (SI_{HCC}), the liver parenchyma without cirrhosis (SI_{liver}), the liver parenchyma with cirrhosis ($SI_{cirrhosis}$), and standard deviation of noise ($S.D._{noise}$), respectively. Signal-to-noise ratio (SNR) was then calculated on both pre- and post-SPIO-alginate images by taking the SI_{HCC}, SI_{liver} or $SI_{cirrhosis}$ dividing by each $S.D._{noise}$. In addition, contrast-to-noise ratio (CNR) was calculated with the following formula: $(SI_{HCC} - SI_{cirrhosis})/S.D._{noise}$, and the relative contrast was expressed as $SI_{HCC}/SI_{cirrhosis}$.

3. Results

3.1. Pharmacokinetics of SPIO-alginate in normal rats

After injection of SPIO-alginate at both low dose and high dose, the blood iron concentration first gradually decreased from the maximal concentration at 0.083 h to the lowest concentration at 48 h (from 515.5 to 266.3 μg/mL for SPIO-low dose group, and from 647.7 to 333.6 μg/mL for SPIO-high dose group, respectively), and then recovered to the initial concentration before injection (about 471.9 μg/mL) at 96 h. In addition, the blood iron concentration after injection of alginate solution and saline also showed the similar profile (mildly down and up), and

Table 1
Serum iron concentration in rats after intravenous injection of SPIO-low dose (109.5 μmol Fe/kg), SPIO-high dose (218.9 μmol Fe/kg), 1 mL 0.6% (w/v) alginate solution, and saline. The basic serum iron concentration before administration was 10.64 ± 4.58 μg/mL. Data represent mean ± S.D.

Time (h)	SPIO-low dose	SPIO-high dose	Alginate solution	Saline
0	9.32 ± 5.55	9.08 ± 3.42	10.96 ± 4.73	21.09 ± 6.13
0.083	143.75 ± 18.61	356.10 ± 42.82	6.16 ± 1.52	15.75 ± 3.71
0.167	131.90 ± 13.56	310.44 ± 64.55	5.48 ± 0.57	15.01 ± 1.18
0.5	57.62 ± 19.43	183.87 ± 37.37	7.49 ± 0.88	17.23 ± 2.23
1	19.57 ± 10.82	108.28 ± 38.23	8.52 ± 3.07	10.80 ± 1.88
3	8.74 ± 5.29	19.83 ± 15.31	6.86 ± 2.08	12.51 ± 5.25
6	6.79 ± 3.20	8.68 ± 5.36	4.72 ± 1.61	9.71 ± 0.92
12	3.28 ± 1.01	3.89 ± 2.13	6.96 ± 3.54	6.48 ± 1.23
24	4.52 ± 1.43	3.01 ± 1.75	5.07 ± 1.29	ND

ND: not determined.

the blood iron concentrations in all rats were even under the initial concentration before injection between 6 and 48 h after injection.

The basic serum iron concentration before administration fluctuated between 6.06 and 15.22 μg/mL. The serum iron concentrations at various time points after injection of alginate solution and saline located in the range of basic serum iron concentration (Table 1). But, the serum iron concentrations increased significantly after SPIO-alginate injection and then decreased to the basic serum iron concentration range at 3 h for low dose and at 6 h for high dose. The $T_{1/2}$ of SPIO-alginate was 0.27 ± 0.06 h at low dose and 0.65 ± 0.22 h at high dose calculated by noncompartmental analysis (Table 2).

3.2. Tissue distribution of SPIO-alginate in normal rats

Table 3 showed that the iron concentrations in liver and spleen significantly increased, while those in blood, lungs, heart, and kidneys slightly changed after injection of SPIO-alginate at low dose. Considering the weights of organs, the results revealed that more than 80% of the injected iron accumulated into the liver, and about 10% into the spleen while less than 2% was found in the kidneys, heart and lungs, respectively. The iron concentrations in the liver and the spleen were high between 0.5 and 24 h, and began to decrease after 24 h. The tissue distribution parameters in liver and spleen for SPIO-alginate in rat calculated by the WinNonlin program using noncompartmental model was given in Table 2. It indicated that the elimination of iron in liver was slower than that in spleen.

3.3. Histological evaluation in normal rat

Although the experiments were carried out at different time points before and after injection of SPIO-alginate as described in methods, only the typical micrographs were shown in order to shorten the length of writing. HE staining could reflect the effect of SPIO-alginate on the morphology of tissues. The sections indicated that there was no significant change on the basic structure of all the specimens of liver and spleen, though there was a little edema of hepatocytes in the perimeter section of liver lobules (Fig. 1).

Perls staining was performed to detect the iron particles dyed blue. Stainable iron was observed in KCs in hepatic sinusoid, in splenic cord of the perimeter section of follicle and in splenic red pulp at 0.5, 24, 96, and 336 h after injection of low dose of SPIO-alginate (Fig. 1). Additionally, iron particles were distributed in the perimeter section of liver lobules at 0.5 h and in the center section at 96 h. The amount of iron oxide particles in liver qualitatively peaked between 0.5 and 24 h after injection, and small amounts of particles were still present at 336 h after injection. The results in the spleen were similar to those in the liver.

Table 2
Serum, liver and spleen parameters of SPIO-alginate in rats following intravenous injection at 109.5 and 218.9 μmol Fe/kg using noncompartmental analysis with bolus IV administration for serum and extravascular administration for liver and spleen

Parameters	Serum ($n = 5$)		Liver	Spleen
	Low dose	High dose	Low dose	Low dose
T_{max} (h)	0.083	0.083, 0.176	0.5	24
C_{max} (μg/mL or g)	147.91 ± 20.72	348.99 ± 43.78*	176.64	290.06
λ (h^{-1})[a]	2.95 ± 0.87	1.28 ± 0.40*	0.005	0.0085
$AUC_{0\to 24h}$ (h μg/mL or h μg/g)[b]	68.37 ± 18.87	321.74 ± 123.72*	35,176.83	26,307.97
$T_{1/2}$ (h)	0.25 ± 0.06	0.59 ± 0.20*	139.19	81.98
$MRT_{0\to 24h}$ (h)	0.32 ± 0.11	0.76 ± 0.27*	181.179	86.235

Each value of serum parameter represents the mean ± S.D.
[a] $T_{1/2}$ was calculated from the terminal slope by means of log-linear regression.
[b] AUC was calculated by linear trapezoidal rule.
* $P < 0.05$, compared with the value of low dose in serum.

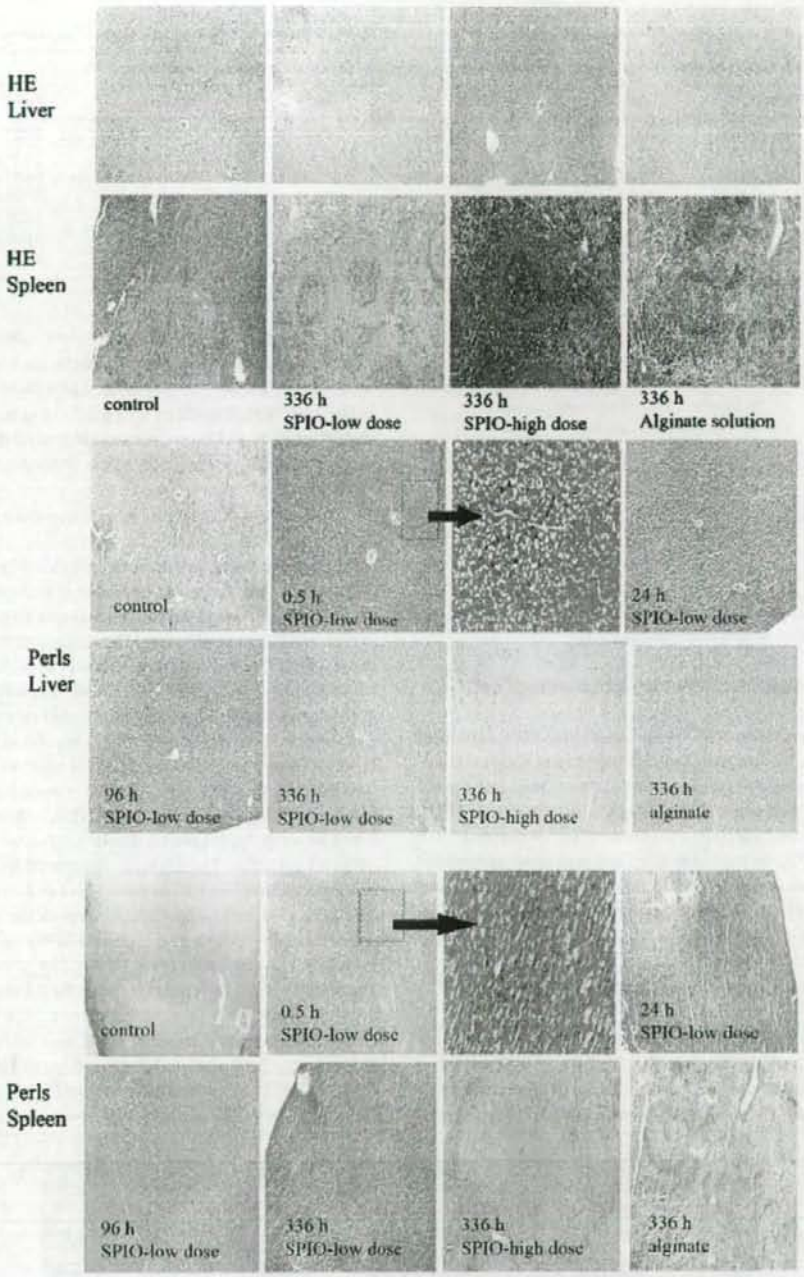

Fig. 1. Sections of liver and spleen of normal rat with HE staining and Perls staining (magnification ×10).

Table 3
Iron concentration in different tissues at different timepoints after intravenous injection of SPIO-low dose (109.5 μmol Fe/kg). Data represent mean ± S.D. ($n=3$)

Time (h)	Iron concentrations in tissue (μg Fe/mL in whole blood; μg Fe/kg in heart, liver, spleen, lung, and kidney)					
	Whole blood	Liver	Spleen	Lung	Kidney	Heart
0	471.93 ± 55.06	58.42 ± 7.56	112.22 ± 24.69	56.67 ± 9.54	52.01 ± 8.61	59.61 ± 13.38
0.5	439.31 ± 54.98	235.05 ± 19.62	350.46 ± 51.17	60.20 ± 14.84	47.23 ± 9.95	59.56 ± 7.07
3	342.28 ± 68.38	199.22 ± 19.69	353.72 ± 144.36	55.40 ± 11.95	41.93 ± 3.73	66.03 ± 19.40
24	313.44 ± 113.85	226.57 ± 38.78	402.28 ± 187.31	79.25 ± 10.67	48.64 ± 9.36	51.28 ± 4.48
48	266.34 ± 27.49	191.45 ± 33.44	247.70 ± 18.61	71.47 ± 13.58	45.96 ± 4.06	58.56 ± 5.04
96	402.88 ± 96.96	159.99 ± 9.16	176.21 ± 27.11	63.05 ± 1.98	44.29 ± 4.87	51.87 ± 5.37
336	552.05 ± 36.63	89.76	122.68	45.45	55.24	40.08

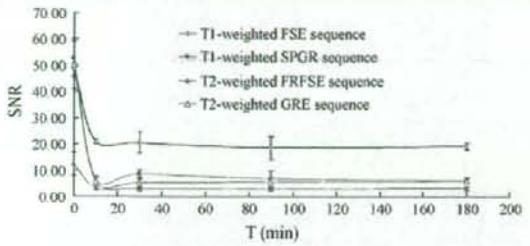

Fig. 2. *In vivo* SNR of liver in normal rats after injection of SPIO-alginate at a dose of 20 μmol Fe/kg. A negative enhancement was observed with T1-weighted, T2-weighted, and T2*-weighted sequences.

3.4. Liver enhancement of SPIO-alginate in normal rat

Fig. 2 showed the liver SNR before and after SPIO-alginate injection on both T1-weighted and T2-weighted images. Compared with unenhanced images ($t=0$), the SNR decreased at 10 min on T1-weighted FSE images, T1-weighted SPGR images, T2-weighted FRFSE images, and T2*-weighted GRE images, after SPIO-alginate injection, and remained almost stable up to 180 min, respectively. Hence, a remarkable negative enhancement was immediately obtained after the injection of SPIO-alginate.

3.5. MR imaging for rabbit tumor model

Fig. 3 showed the MR signal intensity of liver parenchyma (thick arrow) decreased, however, that of the tumor (fine arrow) did not obviously change and the borderline of the tumor was found more clearly in comparison with that of unenhanced image. The photograph and sections of rabbit VX2 tumor with Perls staining after MR imaging enhanced with SPIO-alginate were shown in Fig. 4. It was evident that there was a single tumor in the liver with the size of about 2.5 cm in accordance with that in MR images in Fig. 3. Iron oxide particles were observed in the normal part of liver rather than in the tumor (Fig. 4).

3.6. MR imaging for rats with primary liver cancer

During the process of establishing primary liver cancer model of rats, eight rats were dead because of hemorrhage in the tumor and poor resistance. In addition, two rats were chosen randomly and identified as cirrhosis at 12 weeks, and four rats were identified as HCC with cirrhosis at 15 weeks from MR imaging and pathological evaluation. Fifteen rats survived at 18 weeks in MR imaging experiment. All the fifteen rats were accompanied with severe cirrhosis, and no HCC was found in any rat on MR images before the injection of SPIO-alginate (pre-SPIO, unenhanced imaging). However, 22 HCCs were found in 11 rats after injection of SPIO-alginate (post-SPIO, enhanced imaging) and four rats were diagnosed as simple cirrhosis even after injection of SPIO-alginate. The SNR_{liver} decreased from 48.95 ± 4.87 at pre-SPIO to 6.43 ± 3.37 at post-SPIO and the $SNR_{cirrhosis}$ from 45.51 ± 11.71 to 23.47 ± 7.52. However, the SNR_{HCC} remained almost stable (45.51 ± 11.71 at pre-SPIO and 40.53 ± 12.98 at post-SPIO). Furthermore, the CNR of HCC increased from zero at pre-SPIO to 17.69 ± 3.69 at post-SPIO and the relative contrast increased from 1.0 at pre-SPIO to 1.79 ± 0.31 at post-SPIO. Hence, the contrast between HCC and liver parenchyma was significantly increased and the detection of HCC was improved.

In Fig. 5, compared with the signal intensity on unenhanced T2*-weighted GRE images, the liver signal intensity of nor-

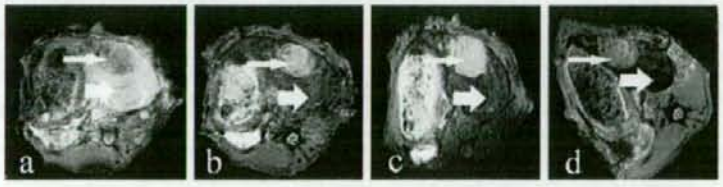

Fig. 3. T2*-weighted FSPGR images (TR/TE, 220 ms/5.2 ms) of xenograft liver cancer in rabbit at (a) 0 min (unenhanced imaging), (b) 10 min, (c) 30 min, and (d) 60 min after intravenous injection of SPIO-alginate at a dose of 20 μmol Fe/kg. After injection of SPIO-alginate, the liver parenchyma (thickness arrow) showed a distinct signal loss, whereas that of the tumor (fine arrow) remained almost unaffected. Hence, the contrast between tumor and liver parenchyma was significantly increased.

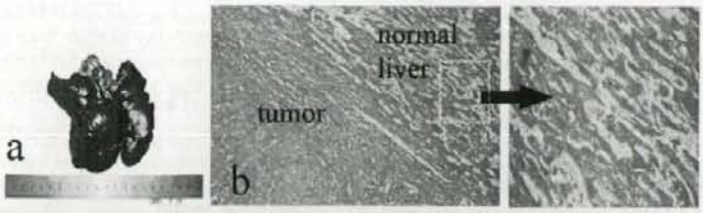

Fig. 4. Photographs (a) and sections of rabbit VX2 tumor with Perls staining (b) after MR imaging enhanced with SPIO-alginate. Iron oxide particles were not found in the tumor part, but in the normal part of the liver (magnification ×10).

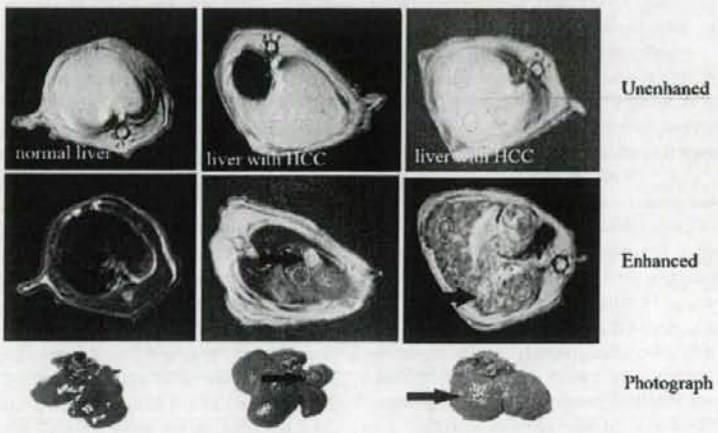

Fig. 5. T2*-weighted GRE images and photographs of liver with primary cancer in rats. No HCC was found on unenhanced images, however, some HCC were found (arrow) on SPIO-alginate enhanced images. The center photograph showed the liver of model rat has one HCC and slight cirrhosis, and the right-hand side photograph showed the liver of model rat has more HCC and severe cirrhosis.

mal rat on enhanced images decreased significantly, slightly decreased for cirrhosis, and almost did not decrease for HCC. Furthermore, there were hyperplastic nodules and some hemorrhage in photographs of model rats' liver. Fig. 6 showed the sections of liver with Perls staining after MR imaging scan, ranging from 2 to 12 h after injection of 20 μmol Fe/kg of SPIO-alginate, which indicated that iron oxide particles were present in normal liver, hyperplastic nodule and hemangioma, rather

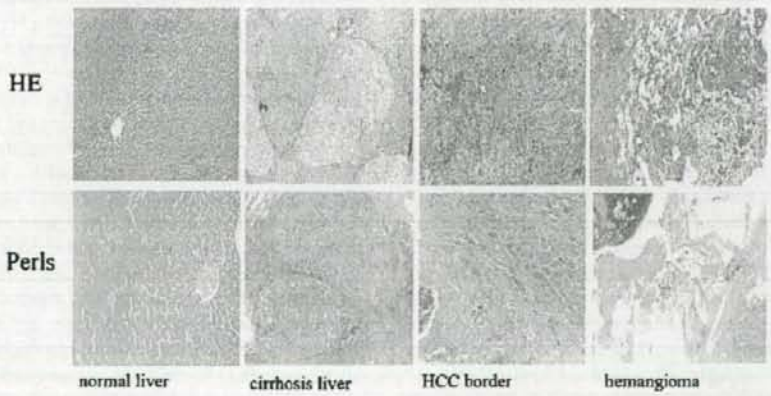

Fig. 6. Light micrograph with HE staining and Perls staining of liver in rats with primary cancer after MR imaging scan within 2–12 h after injection of 20 μmol Fe/kg of SPIO-alginate. According to HE staining, the liver structure of control group was normal, and that of tumor model group accompanied with cirrhosis. Besides HCC, hyperplastic nodule, and hemangioma were identified. As for Perls staining, iron oxide particles were detected in the hemangioma and hyperplastic nodule, rather than in HCC (magnification ×10).

than in HCC. All the livers of model rats were accompanied by cirrohsis according to HE staining. Meanwhile, some HCCs, hyperplastic nodules, and hemangiomas were indentified.

4. Discussion

The alginate used in the study is of pharmaceutical grade which has been approved for oral administration as an inactive ingredient in human. Moreover, sodium alginate was studied for intravenous injection in some animals, and the LD_{50} was described as less than 200 mg/kg for mouse, approximately 100 mg/kg for rabbit (Solandt, 1941), and 1000 mg/kg for rat (Sokov, 1970). In this study, the amounts of sodium alginate used in rats were about 40 mg/kg, which is far less than the LD_{50} (Sokov, 1970). Furthermore, alginate is considered biocompatible and biodegradable in tissues. Alginate has been reported to undergo proton catalyzed hydrolysis which is dependent on time, pH, and temperature (Gombotz and Wee, 1998; Bouhadir et al., 2001; Robitaille et al., 1999). In addition, the chemical composition and the mitogenic contaminants found in alginate are the two main contributors to alginate immunogenicity including cytokine release and inflammatory reactions (Gombotz and Wee, 1998). Hence, the degradatioin of alginate in SPIO-alginate might result in the edema of hepatocytes.

Pharmacokinetics and tissue distribution of SPIO-alginate after intravenous injection were quantitatively studied by determining the iron concentration in blood, serum and tissues. Although it was difficult to differentiate between the endogenous iron and the injected iron, it was reliable to reflect the *in vivo* behavior of SPIO-alginate by subtracting the endogenous iron concentration and this method was used in some studies (Taupitz et al., 2004; Bourrinet et al., 2006). The phenomenon that the blood iron concentration values were under the initial concentration before injection (about 471.9 μg/mL) was observed from about 6 to 48 h after administration of SPIO-alginate, alginate solution and saline, was speculated these might be caused by the several bleedings. After several bleedings, red blood cell count would decrease and therefore there would be a decrease in iron content in blood samples. The blood iron concentration began to increase to initial level at 96 h after injection for both SPIO-alginate, which might be resulted from the fact that SPIO-alginate after uptake by macrophages was degraded by the lysosomes, and then the iron entered the plasma iron pool and was subsequently incorporated into red cell production (Pouliquen et al., 1991; Weissleder et al., 1989).

Since blood loss could significantly decrease red blood count and blood iron concentration, it was better to evaluate the pharmacokinetics of SPIO-alginate in serum, even though the basic serum iron concentration fluctuated according to different rats. In our study, the serum iron concentrations at various time points after injection of alginate solution were in the range of basic serum iron concentration (Table 1). Hence, it indicated that the intravenous injection of alginate solution had no effect on serum iron concentration. We speculated that the COO^- terminals of alginate might not bind the iron in serum. On the other hand, the half-life of SPIO-alginate in serum were 0.27 ± 0.05 h at 109.5 μmol Fe/kg and 0.65 ± 0.22 h at 218.9 μmol Fe/kg in rats in Table 2. C_{max}, $T_{1/2}$, AUC and MRT in serum with the high dose were significantly higher than those of the low dose ($P < 0.05$). After intravenous injection, SPIO-alginate accumulated dominantly in the liver and spleen with a total percentage of more than 90% (Table 3).

As an MR contrast agent, the physicochemical properties including the size of the particle, the charge and the nature of the coating, and the dose will determine the stability, distribution and metabolism of SPIO agents, and then will certainly affect MR imaging (Gupta and Gupta, 2005; Wang et al., 2001; Neuberger et al., 2005). According to the previous studies, the particle size played a very important role. The larger the particles, the shorter the plasma half-life is (Wang et al., 2001). Since SPIO uptake into the RES is related to protein absorption on the particle surface and subsequent opsonization, minimizing the particle size will ultimately reduce particle phagocytosis, finally resulting in a significant increase in plasma half-life and wider biodistribution (Neuberger et al., 2005). Although SPIO-alginate used in this research had a mean core diameter of about 5–10 nm, the big hydrodynamic diameter of 193.8 nm and high negative ξ-potential might explain the fast clearance from blood and the accumulation mostly in the liver and spleen (Table 2). This result was in accordance with the report that the blood half-life of Ferumoxides was 6 min and efficiently accumulated in the liver (approximately 80% of the injected dose) and spleen (5–10% of the injected dose) with minutes of administration (Wang et al., 2001). The amount of iron oxide (about 10–20 μmol Fe/kg body weight) for clinical MR imaging is small compared with other MR contrast agents and extensive toxicity studies in animals have indicated no acute or chronic toxicity at doses greater than 100 times the clinical effective dose (Weissleder et al., 1989; Reimer et al., 1995).

For specific characterization of liver lesions, the tissue-specific contrast agent should be located predominantly in one tissue. The distribution of contrast agent in liver is rather complicated, as it can be located in the extracellular space including blood and interstitium, and cellular space including reticuloendothelial cells, hepatocytes and endothelial cells. In our study, Perls staining did not show iron within hepatocytes but mainly within the KCs. Furthermore, the account of SPIO-alginate in the liver peaked at 0.5 h with the dose of 109.5 μmol Fe/kg from quantitative iron concentration (Table 3) and qualitative histology evaluation (Fig. 1). This suggested that SPIO-alginate could not act as an extracelluar agent during the early time points. These results were in accordance with the liver enhancement of SPIO-alginate in normal rat, in which a significant decrease of the liver signal intensity on T1-weighted images at 10 min was observed (Fig. 2). It was reported that positive enhancement on T1-weighted images was observed when the iron particles were extracelluar. When the particles were intracellular, only a negative enhancement was seen (Oswald et al., 1997; Van Beers et al., 2001). It was suggested that the uptake of contrast agents of negative ξ-potential was mediated by scavenger receptors expressed in both Kupffer and liver endothelial cells (Seternes et al., 2001). Compared to KCs, liver endothelial cells were believed to be less effective at metabolizing and degrading particlulate iron (Briley-Sæbø et al., 2004). The half life of SPIO-alginate in

liver at a dose of 109.5 μmol Fe/kg was about 139.1 h (Table 2) and only small iron was observed at 336 h after injection from Perls staining (Fig. 1). Hence, we speculated that there was little or almost no SPIO-alginate in endothelial cell. In sum, the distribution of SPIO-alginate in liver was predominately in KCs, which was just the mechanism of SPIO-alginate to detect liver tumors.

A negative enhancement of the liver was observed on both T1- and T2-weighted images after injection of SPIO-alginate in normal rats (Fig. 2). Compared with the corresponding unenhanced images, SNR on enhanced images decreased by 2.32 times with T1-weighted FSE sequence, 8.02 times with T1-weighted SPGR sequences, 3.88 times with T2-weighted IRFSE sequence, and 8.64 times with T2*-weighted GRE sequence. The negative enhancement on T1-weighted images might be caused by the physical characteristics of the individual nanoparticles. In other words, the high-field magnetization of the iron oxide core could be sufficient to relax water protons effectively, which might attribute to the fact that iron oxide was not simply coated by alginate polymer (Ma et al., 2007). Furthermore, the results also indicated that SPIO-alginate did not agglomerate *in vivo* (Kellar et al., 2002). Meanwhile, the intracellular iron particles mentioned above might be another reason for the negative enhancement on T1-weighted images. On the other hand, the negative enhancement effect of SPIO-alginate on T2- and T2*-weighted images was demonstrated, and GRE images were more sensitive to susceptibility effects than FSE images according to earlier report (Ward et al., 2003).

SPIO-alginate was mainly phagocytosed by liver after intravenous administration as mentioned above. As a result, these particles taken up in liver could accelerate T2 relaxation by creating local inhomogeneities in the magnetic field, causing reduced signal intensity on both T1- and T2-weighted images, but most remarkable decrease on acquisitions with T2*-weighted. In this study, HCC was not found at pre-SPIO on T2*-weighted images, but found at post-SPIO, for the signal intensity of HCC was significantly higher than that of the adjacent liver parenchyma (Fig. 5). Hence, MR imaging with SPIO-alginate enhancement was shown to improve the detection of HCC in the cirrhotic liver compared with unenhanced imaging. Our study confirmed these expectations, as did most published studies of the recent years (Saini et al., 1987; Clement et al., 1991; Nakayama et al., 1998; Imai et al., 2000; Bourrinet et al., 2006).

The efficacy of iron oxide to enhance the transverse relaxation rates ($1/T2^* = R2^*$) in the liver depended upon its initial distribution or uptake into the liver. Factors which may alter the uptake of SPIO particles and the resultant effect on signal intensity include phagocytic activity, clustering of the particles, and local blood flow.

First of all, the change of signal intensity in liver on SPIO enhanced MR imaging is mainly mediated by phagocytic activity. And phagocytic activity is depended on both the number of sinusoidal KCs per unit volume of liver parenchyma (KCs tissue density) and individual KCs function. It is suggested that the number of KCs in dysplastic nodules or in cirrhosis is similar to that in adjacent liver parenchyma, and the number of KCs in HCC decreased as the tumors became less well differentiated (Imai et al., 2000). It has been reported that SPIO-enhanced MR imaging can evaluate the number and function of KCs (Tanimoto et al., 2002). In our studies, iron oxide particles were found in normal liver and hyperplastic nodule, rather than in HCC and VX2 tumor from histological evaluation (Figs. 4 and 6).

It has been reported that the signal intensity changes induced by SPIO may vary according to the spatial distribution of particles and cluster size on relaxation times within KCs in T2*-weighted sequences and T2*-insensitive weighted sequences (Imai et al., 2000). Additionally, large intracellular SPIO clusters produced greater SNR loss on GRE images than small clusters because of the magnetic susceptibility effects relating to fixed-field inhomogeneity. In contrast, small intracellular clusters caused little SNR decrease on T2*-weighted GRE images while the small clusters produced substantial SNR loss on T2-weighted FSE images. This could attribute to T2 shortening mechanisms that were independent of magnetic susceptibility effects but relate to the greater free water interaction made possible by the relatively larger surface area of the small clusters (Tanimoto et al., 1994; Tanimoto et al., 2001). However, the size of the intracellular SPIO clusters depended on individual KC phagocytic function. Hence, impaired phagocytic activity, as in liver cirrhosis, should be associated with a decreased average size of SPIO clusters within KC. In this study, SNR of the normal liver of control rats with T2*-weighted GRE sequence decreased by about eight times on SPIO-enhanced images, while twice as that of the cirrhosis liver of model rats. This result was consistent with those reports that the signal intensity induced by SPIO in patients with liver cirrhosis was less remarkable than that in non-cirrhotic patients (Hundt et al., 2000; Clement et al., 1991; Nakayama et al., 1998). Hemangiomas could show SPIO uptake because of the blood pool effect, although they do not contain KCs (Kim et al., 2002). It was obvious that there were many iron oxide particles stainable in hemangiomas in Fig. 6. Therefore, hemangiomas could not be identified on T2*-weighted MR images.

5. Conclusion

The SPIO-alginate was cleared rapidly from serum with the half-life of 0.27 h at 109.5 μmol Fe/kg and accumulated dominantly in the liver and spleen with a total percentage of more than 90% after intravenous injection. Iron oxide particles in KCs as well as splenic red pulp were observed from histological evaluation in normal rats. The experiments on MR imaging indicated that SPIO-alginate as an MR contrast agent might have the ability to improve detection of liver tumor.

Acknowledgements

This work was supported by funds from National High Technology Research and Development Program of China (2003AA326020), National Basic Research Program of China 2007CB935801, and National Natural Science Foundation of China (30772665).

References

Bouhadir, K.H., Lee, K.Y., Alsberg, E., Damm, K.L., Anderson, K.W., Mooney, D.J., 2001. Degradation of partially oxidized alginate and its potential application for tissue engineering. Biotechnol. Prog. 17, 945–950.

Bourrinet, P., Bengele, H.H., Bonnemain, B., Dencausse, A., Idee, J.M., Jacobs, P.M., Lewis, J.M., 2006. Preclinical safety and pharmacokinetic profile of Ferumoxtran-10, an ultrasmall superparamagnetic iron oxide magnetic resonance contrast agent. Invest. Radiol. 41, 313–324.

Briley-SæbØ, K., Hustvedt, S.O., Haldorsen, A., BjØrnerud, A., 2004. Long-term imaging effects in rat liver after a single injection of an iron oxide nanoparticle based MR contrast agent. J. Magn. Reson. Imaging 20, 622–631.

Clement, O., Frija, G., Chambon, C., Schouman-Clayes, E., Mosnier, J.F., Poupon, M.F., Balkau, B., 1991. Liver tumors in cirrhosis: experimental study with SPIO-enhanced MR imaging. Radiology 180, 31–36.

Corot, C., Robert, P., Idee, J.M., Port, M., 2006. Recent advances in iron oxide nanocrystal technology for medical imaging. Adv. Drug Deliv. Rev. 58, 1471–1504.

Gombotz, W.R., Wee, S.F., 1998. Protein release from alginate matrices. Adv. Drug Deliv. Rev. 31, 267–285.

Gupta, A.K., Gupta, M., 2005. Synthesis and surface engineering of iron oxide nanoparticles for biomedical applications. Biomaterials 26, 3995–4021.

Hagar, W., Vichinsky, E.P., Theil, E.C., 2003. Liver ferritin subunit ratios in neonatal hemochromatosis. Pediatr. Hematol. Oncol. 20, 229–235.

Harmut-Hoene, A., Schelenz, R., 1980. Effect of dietary fiber on mineral absorption in growing rats. J. Nutr. 110, 1774–1784.

Hauff, P., Fritzsch, T., Reinhardt, M., Weitschies, W., Lueders, F., Uhlendorf, V., Heldmann, D., 1997. Delineation of experimental liver tumors in rabbits by a new ultrasound contrast agent and stimulated acoustic emission. Invest. Radiol. 32, 94–99.

Hundt, W., Petsch, R., Helmberger, T., Reiser, M., 2000. Signal changes in liver and spleen after Endorem administration in patients with and without liver cirrhosis. Eur. Radiol. 10, 409–416.

Imai, Y., Murakami, T., Yoshida, S., Nishikawa, M., Ohsawa, M., Tokunaga, K., Murata, M., Shibata, K., Zushi, S., Kurokawa, M., Yonezawa, T., Kawata, S., Takamura, M., Nagano, H., Sakon, M., Monden, M., Wakasa, K., Nakamura, H., 2000. Superparamagnetic iron oxide-enhanced magnetic resonance images of hepatocellular carcinoma: correlation with histological grading. Hepatology 32, 205–212.

Kellar, K.E., Fujii, D.K., Gunther, W.H.H., Briley-Saebo, K., Bjornerod, A., Spiller, M., Koenig, S.H., 2002. Important considerations in the design of iron oxide nanoparticles as contrast agents for T1-weighted MRI and MRA. Acad. Radiol. 9, S34–S37.

Kellar, K.E., Fujii, D.K., Gunther, W.H.H., Briley-Saebo, K., Bjornerod, A., Spiller, M., Koenig, S.H., 2000. "NC100150 injection," a preparation of optimized iron oxide nanoparticles for positive contrast MR angiography. J. Magn. Reson. Imaging 11, 488–494.

Kim, J.H., Kim, M.J., Suh, S.H., Chung, J.J., Yoo, H.S., Lee, J.T., 2002. Characterization of focal hepatic lesions with ferumoxides-enhanced MR imaging: utility of T1-weighted spoiled gradient recalled echo images using different echo times. J. Magn. Reson. Imaging 15, 573–583.

Ma, H.L., Qi, X.R., Maitani, Y., Nagai, T., 2007. Preparation and characterization of superparamagnetic iron oxide nanoparticles stabilized by alginate. Int. J. Pharma 333, 177–186.

Ma, H.L., Qi, X.R., Ding, W.X., Maitani, Y., Nagai, T., 2007a. Magnetic targeting after femoral artery administration and biocompatibility assessment of superparamagnetic iron oxide nanoparticles. J. Biomed. Mater. Res. Part A 84A, 598–606.

Nakayama, M., Kamura, T., Kimura, M., Seki, H., Tsukada, K., Sakai, K., 1998. Quantitative MRI of hepatocellular carcinoma in cirrhotic and noncirrhotic livers. Clin. Imaging 22, 280–283.

Neuberger, T., Schöpf, B., Hofmann, H., Hofmann, M., Von Rechenberg, B., 2005. Superparamagnetic nanoparticles for biomedical applications: Possibilities and limitations of a new drug delivery system. J. Magn. Magn. Mater. 293, 483–496.

Oswald, P., Clement, O., Chambon, C., Schouman-Claeys, E., Frija, G., 1997. Liver positive enhancement after injection of superparamagnetic nanoparticles: respective role of circulating and uptaken particles. Magn. Reson. Imaging 15, 1025–1031.

Pouliquen, D., Le Jeune, J.J., Perdrisot, R., Ermias, A., Jallet, P., 1991. Iron oxide nanoparticles for use as an MRI contrast agent: pharmacokinetics and metabolism. Magn. Reson. Imaging 9, 275–283.

Reimer, P., Rummeny, E.J., Daldrup, H.E., Balzer, T., Tombach, B., Berns, T., Peters, P.E., 1995. Clinical results with resovist: a phase 2 clinical trial. Radiology 195, 489–496.

Robitaille, R., Pariseau, J.F., Leblond, F.A., Lamoureux, M., Lepage, Y., Hallé, J.P., 1999. Studies on small (<350 μm) alginate-poly-L-lysine microcapsules. III. Biocompatibility of smaller versus standard microcapsules. J. Biomed. Mater. Res. 44, 116–120.

Saini, S., Stark, D.D., Hahn, P.F., Bousquet, J.C., Introcasso, J., Wittenberg, J., Brady, T.J., Ferrucci J.T.Jr., 1987. Ferrite particles: a superparamagnetic MR contrast agent for enhanced detection of liver carcinoma. Radiology 162, 217–222.

Seternes, T., Oynebraten, I., Sorensen, K., Smedsrod, B., 2001. Specific endocytosis and catabolism in the scavenger endothelial cells of cod (*Gadus morhua* L.) generate high-energy metabolites. J. Exp. Biol. 204, 1537–1546.

Sokov, L.A., 1970. Radioaktivnye Izotopy Vo Vneshnei Sredei Organizine. Atomizdat, Moscow, p. 247.

Solandt, O.M., 1941. Some observations upon sodium alginate. Quart. J. Exp. Physiol. 31, 25–30.

Tanimoto, A., Pouliquen, D., Kreft, B.P., Stark, D.D., 1994. Effects of spatial distribution on proton relaxation enhancement by particulate iron oxide. J. Magn. Reson. Imaging 4, 653–657.

Tanimoto, A., Oshio, K., Suematsu, M., Pouliquen, D., Stark, D.D., 2001. Relaxation effects of clustered particles. J. Magn. Reson. Imaging 14, 72–77.

Tanimoto, A., Yuasa, Y., Shinmoto, H., Jinzaki, M., Imai, Y., Okuda, S., Kuribayashi, S., 2002. Superparamagetic iron oxide-mediated hepatic signal intensity change in patients with and without cirrhosis: pulse sequence effects and Kupffer cell function. Radiology 222, 661–666.

Taupitz, M., Wagner, S., Schnorr, J., Kravec, I., Pilgrimm, H., Bergmann-Fritsch, H., Hamm, B., 2004. Phase I clinical evaluation of citrate-coated monocrystalline very small superparamagnetic iron oxide particles as a new contrast medium for magnetic resonance imaging. Invest. Radiol. 39, 394–405.

Van Beers, B.E., Sempoux, C., Materne, R., Delos, M., Smith, A.M., 2001. Biodistribution of ultrasmall iron oxide particles in the rat liver. J. Magn. Reson. Imaging 13, 594–599.

Wang, Y.X., Hussain, S.M., Krestin, G.P., 2001. Superparamagnetic iron oxide contrast agents: physicochemical characteristics and applications in MR imaging. Eur. Radiol. 11, 2319–2331.

Ward, J., Guthrie, J.A., Wilson, D., Arnold, P., Lodge, P., Toogood, G.J., Wyatt, J.I., Robinson, P.J., 2003. Colorectal hepatic metastases: detection with SPIO-enhanced breath-hold MR imaging-comparison of optimized sequences. Radiology 228, 709–718.

Weinmann, H.J., Ebert, W., Misselwitz, B., Schmitt-Willich, H., 2003. Tissue-specific MR contrast agents. Eur. J. Radiol. 46, 33–44.

Weissleder, R., Stark, D.D., Engelstad, B.L., Bacon, B.R., Compton, C.C., White, D.L., Jacobs, P., Lewis, J., 1989. Superparamagnetic iron oxide: pharmacokinetics and toxicity. Am. J. Roentgenol. 152, 167–173.

Available online at www.sciencedirect.com
ScienceDirect
Journal of Controlled Release 127 (2008) 231–238
journal of controlled release
www.elsevier.com/locate/jconrel

In vivo antitumor activity of camptothecin incorporated in liposomes formulated with an artificial lipid and human serum albumin

Masato Watanabe [a], Kumi Kawano [a], Kazunori Toma [b], Yoshiyuki Hattori [a], Yoshie Maitani [a,*]

[a] Institute of Medicinal Chemistry, Hoshi University, Ebara 2-4-41, Shinagawa-ku, Tokyo 142-8501, Japan
[b] The Noguchi Institute, Kaga 1-8-1, Itabashi-ku, Tokyo 173-0003, Japan

Received 12 October 2007; accepted 10 February 2008
Available online 20 February 2008

Abstract

Camptothecin (CPT) is a strong antitumor agent, but its use limited by its low solubility and the instability of the active lactone form. To overcome these difficulties, liposomes incorporating CPT (CPT liposomes) were designed and tested. CPT liposomes were formulated by the addition of 3,5-bis(dodecyloxy)benzoic acid (DB) to polyethylene glycol-containing liposomes, and by coating the surface of the liposomes with human serum albumin (HSA, HSA-DB-L). HSA-DB-L successfully entrapped CPT with about 80% efficiency and with a particle size of about 150 nm. HSA-DB-L showed attenuated drug release and storage stability. Pharmacokinetics studies in mice showed that i.v. injection of HSA-DB-L (2.5 mg/kg) led to prolonged circulation in the plasma; the area under the curve was 22-fold higher than that of CPT solution. The tumor growth in mice with subcutaneous transplantation of colon 26 tumor cells was significantly inhibited after a single i.v. injection of HSA-DB-L at a dose of 15 mg/kg without any significant body weight loss. HSA-DB-L increased the accumulation of CPT in tumor tissue significantly (9.6-fold) more efficiently than CPT solution 24 h after i.v. injection. These findings suggest that HSA-DB-L could increase the stability and the antitumor effect of CPT. CPT delivery by novel liposome formulations is a potential approach for effective treatment of cancer.

Keywords: Camptothecin; Liposome; Antitumor effect; HSA; Colon 26 tumor

1. Introduction

Camptothecin (CPT) is a naturally occurring cytotoxic alkaloid isolated from the Chinese plant *Camptotheca accuminata* [1]. CPT and some of its analogs have shown a broad spectrum of antitumor activity against many solid tumors in xenografts, including colorectal cancer [2,3]. CPT inhibits the enzyme DNA topoisomerase I, initially by noncovalent binding and subsequently by stabilization of the complex through a nucleophilic attack by the enzyme at the acyl position of the CPT lactone ring [4]. Under physiological conditions, i.e., at pH 7 or above, the lactone ring readily opens to yield the inactive carboxylate form of the drug, and this conversion is in pH-dependent equilibrium [5] (Fig. 1(A)). Moreover, the presence of human serum albumin (HSA) in the blood or serum showed rapid CPT lactone ring opening. This was probably due to preferential HSA binding to the carboxylate form resulting in a change in the lactone-carboxylate equilibrium. Thus shifts the equilibrium toward the pharmacologically ineffective carboxylate form [6]. Only the lactone form of CPT is biologically active; however, this form exhibits poor aqueous solubility.

To overcome these stability and solubility problems of CPT, several approaches have been investigated. In addition to the synthesis of new derivatives and pro-drug products [7,8], the development of adequate drug carriers is gaining increasing attention. There are many reports about effective formulation and utilization of CPT in cancer therapy by using drug delivery technologies such as incorporation in liposomes [9,10], polymer micelles[11,12], microemulsions [10], and microspheres [13,14]. About liposomes, the protection of the lactone form of CPT by liposomes has been known [9]. Low solubility of CPT in water or lipids, however, was limited to develop liposomal CPT. Safer and more water-soluble CPT derivatives, therefore,

* Corresponding author. Tel./fax: +81 3 5498 5048.
E-mail address: yoshie@hoshi.ac.jp (Y. Maitani).

0168-3659/$ - see front matter © 2008 Elsevier B.V. All rights reserved.
doi:10.1016/j.jconrel.2008.02.005

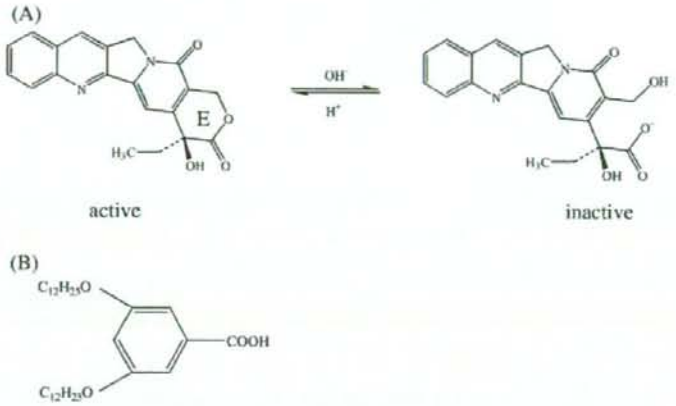

Fig. 1. Structure of camptothecin (CPT) and equilibrium reaction between the active and inactive form (A) and structure of 3,5-bis(dodecyloxy)benzoic acid (DB).

were used to be entrapped in the liposomal water phase [15,16]. CPT has higher activity than these derivatives [17]. If stable CPT liposomal formulations in vivo can be developed, high antitumor effect will be obtained.

To this purpose, novel CPT liposomes were formulated by the addition of an artificial lipid with a phenyl group to polyethylene glycol-modified liposomes, and by coating the surface of the liposomes with HSA. Because we reported that stable CPT-loaded polymer micelles in vivo were produced using benzyl polymer [11,12,18,19], presumably due to be $\pi-\pi$ interaction of the phenyl group with CPT, lipids with a phenyl group in liposomes might interact with CPT and could incorporate CPT effectively. An artificial lipid with a phenyl group, 3,5-bis (dodecyloxy) benzoic acid (DB), therefore, was synthesized (Fig. 1(B)) and added to the liposome formulation. We also modified liposomes with polyethylene glycol (PEG) for long circulating, because they can passively deliver chemotherapeutic agents to tumor sites via the enhanced permeation and retention (EPR) effect [20–22]. Furthermore, we coated the liposomes by HSA because pre-coating polystyrene particles with HSA enhanced their stability in blood [23].

In the present study, we demonstrated that CPT could be efficiently incorporated into the pegylated liposomes by the addition of DB, combined with coating HSA on the surface of the liposomes. The drug release from the liposomes, the storage stability, pharmacokinetics, and in vivo antitumor activity of HSA-DB-L were examined. The liposomal form of CPT displayed antitumor activity against mice bearing colon adenocarcinoma 26 when administered by a single i.v. injection.

2. Materials and methods

2.1. Materials

(*S*)-(+)-Camptothecin (CPT), cholesterol (Ch), high performance liquid chromatography (HPLC) grade acetonitrile and triethylamine acetate were purchased from Wako Pure Chemical Industries, Ltd. (Osaka, Japan). Hydrogenated soybean phosphatidylcholine (HSPC, >90% phosphatidylcholine), distearolyphosphatidylethanolamine-*n*-[methoxy(polyethylene glycol)-2000] (PEG2000), distearolyphosphatidylethanolamine-*n*-[methoxy(polyethylene glycol)-5000] (PEG5000) and oleic acid (OA) were purchased from NOF Corporation (Tokyo, Japan). HSA was purchased from Sigma Chemical Co. (St. Louis, MO, USA). DB was synthesized as reported previously [24]. Other chemicals were of reagent grade.

2.2. Preparation of liposomes

CPT-incorporating liposomes (CPT liposomes) composed of the formulations summarized in Table 1 were prepared by a lipid-film hydration method. Briefly, CPT (1 mg) and lipids (e.g., 30 mg of total lipids for DB-L, HSPC/Ch/OA/DB/PEG2000= 7:3:1:1:0.4 (molar ratio)=19.3/4.1/1.0/1.7/3.9 (mg)) were dissolved in a mixture of chloroform: methanol (4:1, volume ratio), and the solvent was removed by evaporation under nitrogen gas flow. The lipid film was hydrated with 2 mL of phosphate-buffered solution (pH 6.0, 2.33% KH_2PO_4: 1.44% $NaHCO_3$=4:1, volume ratio). The lipid mixture was sonicated for 30 min using an ultrasonic bath. Excess CPT was precipitated and could be separated from the liposomes by centrifugation at 1400 ×g for 10 min. Liposomes with average sizes ranging from 150 to 200 nm with low polydispersity index (<0.3) were obtained, as determined using a dynamic light scattering particle size analyzer, and surface potentials of them were determined by the electrophoresis light scattering method (ELS-800, Otsuka Electronics Co., Ltd. Osaka, Japan) at 25 °C by diluting liposome suspensions to an appropriate volume with water.

Good and reproducible recovery of liposomes in the supernatant (>80%) was obtained, as determined by an enzymatic assay using a Phospholipid C-test Wako (Wako Pure Chemical Industries, Ltd.).

Control liposomes (Control-L) were composed of HSPC, Ch, OA and PEG2000. Control-L containing 8 mol% and 15 mol% DB are hereafter designed as DB-L and 2DB-L, respectively. DB-L5000 had a similar composition as DB-L, but contained PEG5000 instead of PEG2000. For coating of DB-L with HSA (HSA-DB-L), the DB-L suspension (e.g., 7.5 mg total lipids/mL)

Table 1
Characterization of CPT liposomes

Code	Formulation (molar ratio)	Particle size (nm)	Incorporation efficiency[a] (%)	% Injected dose in plasma after 4 h[b]
CPT solution		–	–	0.02±0.01
Control-L	HSPC/Ch/OA/PEG2000 (7:3:1:0.4)	137.4±15.4	75.6±11.4	0.3±0.1
DB-L	HSPC/Ch/OA/DB/PEG2000 (7:3:1:1:0.4)	148.4±0.9	80.7±8.4	1.0±0.2
2DB-L	HSPC/Ch/OA/DB/PEG2000 (7:3:1:2:0.4)	177.2±50.5	76.9±16.9	0.04
DB-L5000	HSPC/Ch/OA/DB/PEG5000 (7:3:1:1:0.4)	148.4±0.9	85.8±4.9	0.2±0.2
HSA-DB-L	HSPC/Ch/OA/DB/PEG2000 (7:3:1:1:0.4)+HSA	161.3±9.2	85.8±4.9	2.5±0.8

Each value represents the mean±SD. ($n=3$).
*$P<0.05$, **$P<0.01$, ***$P<0.001$.
[a]Prepared at a feeding ratio of 1/30 (CPT/total lipid, w/w).
[b]Results at a dose of 2.5 mg CPT/kg in ddY mice.

was incubated with 4% HSA aqueous solution at room temperature (20–25 °C) for 1 h. HSA-DB-L was used without separation of free HSA in in vivo experiment.

The CPT solution was prepared by dissolving CPT (13.0 mg) in 50 mL of polyethylene glycol 400, propylene glycol and polysorbate 80 (40:50:2, volume ratio) [25].

2.3. Determination of HSA amount associated with HSA-DB-L

The adsorbed HSA was measured using bicinchoninic acid (BCA) protein assay reagent (Pierce, Rockford, IL, USA) and analyzed by 10% SDS-polyacrylamide gel electrophoresis (SDS-PAGE) after separation of liposomes by ultracentrifugation (100,000 ×g, 1 h, 4 °C). The gel was stained with Coomassie brilliant blue (Quick-CBB, Wako Pure Chemical Industries, Ltd., Osaka, Japan).

2.4. Cytotoxicity of liposomes containing DB

Mouse colon adenocarcinoma 26 (C26) cells (5.0×10^3 cell/well) were plated into 96-well culture plates 1 day before the experiment. The cells were incubated for 48 h at 37 °C with liposomes. The cytotoxicity was then determined using a WST-8 assay (Cell Counting Kit-8, Dojindo Laboratories, Kumamoto, Japan). The number of viable cells was determined by measuring the absorbance at 450 nm on an automated plate reader.

2.5. Determination of efficiency of CPT incorporation into liposomes

Drug incorporation efficiency was determined using the ultracentrifugation method. CPT liposomes were centrifuged at 52,000 ×g for 1 h at 4 °C to separate free CPT from liposomal CPT. Then, the incorporation efficiency was obtained using two methods: determination of the CPT concentration of the supernatant containing free CPT, and determination of the amount of CPT entrapped in the precipitate, which was disrupted using chloroform. The incorporation efficiencies estimated using both methods were similar. The former method was used in the following experiment. The total drug concentrations in liposomes before centrifugation (drug initial) and in the supernatant after centrifugation (drug supernatant) were determined using a fluorescence spectrophotometer (F-4010, Hitachi Electronics, Tokyo, Japan) with excitation and emission wavelengths of 369 and 437 nm, respectively. The percentage of the drug entrapped in the liposomes was calculated as follows:

$$\text{Incorporation efficiency (\%)} = \left(\text{drug}_{\text{initial}} - \text{drug}_{\text{supernatant}}\right)/\text{drug}_{\text{initial}} \times 100.$$

2.6. In vitro drug release of CPT liposomes

In vitro release of CPT from the liposomal formulation was analyzed by membrane dialysis against phosphate-buffered saline (PBS, pH 7.4) at 37 °C under sink condition. Briefly, 1 mL of CPT liposomes (0.4–0.5 mg CPT/mL) was placed in a dialysis tube (Spectra/Por CE, MWCO 300,000, Spectrum Laboratories, Inc., Rancho Dominguez, CA, USA) and then suspended in a temperature-controlled, jacketed flask containing 100 mL of PBS. After various time intervals, aliquots of the medium were withdrawn and assayed for CPT content by fluorophotometry.

2.7. Storage stability study

The lactone form of CPT in the HSA-DB-L was evaluated after storage at room temperature (20–25 °C) for an extended period of time. The lactone and carboxylate forms of CPT liposomes were then immediately measured by reverse-phase HPLC analysis.

The HPLC analysis was performed at room temperature. A Shimadzu LC-10AT (Shimadzu Co., Ltd., Japan) apparatus equipped with a Shimadzu RF-10AXL fluorescence detector in which the excitation and emission wavelengths were set at 369 and 437 nm, respectively, was used. Separation was performed with a Tosoh TSK-gel ODS-80Ts column (150×4.6 mm I.D.).

Table 2
Cytotoxicity of CPT liposomes to colon 26 cells

Code (formulation)	IC50 (μg/mL)
Control-L not containing CPT (HSPC/Ch/OA/PEG2000)	1.1 mg/mL[a]
DB-L not containing CPT (HSPC/Ch/OA/PEG2000)	1.1 mg/mL[a]
CPT solution	0.077
DB-L (HSPC/Ch/OA/DB/PEG2000)	0.048
HSA-DB-L (HSPC/Ch/OA/DB/PEG2000+HSA)	0.042

[a] Concentration of lipids.

The mobile phase was composed of 23:77 (v/v) acetonitrile-triethylamine acetate buffer (1% (v/v), adjusted to pH 5.5 with glacial acetic acid), and the flow rate was set at 1.0 mL/min [26].

2.8. Measurement of CPT concentration in plasma in mice

CPT liposomes or CPT solution was intravenously (i.v.) administered to male ddY mice (weighing 18–20 g, Tokyo Laboratory Animal Science Co., Ltd. Tokyo, Japan) via the lateral tail veins at a dose of 2.5 mg/kg (0.1–0.2 mL/10 g body weight). At various times after the administration, blood was withdrawn using a heparinized syringe and centrifuged at 15,300 ×g for 4 min to obtain the plasma. Plasma was added to 0.1 mL of 0.15 M aqueous phosphoric acid followed by mixing [27] and CPT was extracted with 0.8 mL of chloroform: methanol (4:1, volume ratio). This operation gave the total concentration of free CPT and CPT incorporated into liposomes as a lactone form. After centrifugation of the mixture at 15,300 ×g for 4 min, 25 μL of the organic solvent layer was directly injected into the HPLC system to determine the concentration of CPT. The area under the concentration curve (from 0 h to 24 h: AUC) and clearance were calculated using the bootstrap method [28].

2.9. Biodistribution studies in tumor-bearing mice

At 1 week after transplantation of 1.0×105 cells, when tumor size reached approximately 100 mm^3, C26-bearing CDF1 female mice (6 weeks old) were injected via a lateral tail vein with HSA-DB-L or CPT solution at a dose of 2.5 mg/kg as CPT. After 24 h, the mice were anesthetized with diethyl ether. Blood samples were collected and then the major organs and tumor were excised, rinsed in physiologic saline, weighed, and frozen at −20 °C. The tissues were homogenized in 5.0 mL of PBS. CPT was extracted from tissue homogenate or plasma as described above and the CPT concentration was determined by HPLC.

2.10. In vivo antitumor activity

The antitumor activity against a solid tumor was evaluated with C26. C26 cells (1.0×10^5 cells in 0.2 mL) were transplanted subcutaneously into the backs of CDF1 female mice (5 weeks old, Sankyo Labo Service Corporation, Tokyo, Japan). Drug injection was started 2 weeks after tumor transplantation, when the tumor volume reached approximately 100 mm^3 (Day 0), by i.v. injection via a lateral tail vein. CPT solution was used as a single injection at a dose of 1.5 mg/kg, and HSA-DB-L (e.g., 2.5 mg CPT and 25 mg total lipid/mL) as a single injection at a dose of 10 or 15 mg/kg, and a repeated injection of 10 mg/kg. The control group was injected with 0.9% NaCl solution (0.1 mL/10 g body weight). Tumor volumes and body weights were measured at intervals of a few days. Tumor volume was calculated as follows: volume$=1/2LW^2$; L is the long diameter and W is the short diameter of a tumor. Percent tumor growth inhibition ($T/C\%$) was calculated from the relative tumor volume at day 8 following the equation: $T/C\% = 100 \times$(mean relative tumor volume of treated group)/(mean relative tumor volume of control group). The animal experiments were done with ethical approval from our Institutional Animal Care and Use Committee.

2.11. Statistical analysis

The results were analyzed statistically using Student's t-test. A P-value of 0.05 or less was considered significant.

3. Results

3.1. Characterization of CPT liposomes

To obtain CPT liposomes that were stable in vivo, liposomes were prepared using various formulations by adding DB as a lipid containing a phenyl group and by coating with HSA. The use of DB as a liposome component had not previously been reported, so first the cytotoxicity of DB was evaluated in cell culture. The 50% cell growth inhibitory concentration (IC_{50}) of DB-L and Control-L not containing CPT was 1.1 mg lipid/mL, indicating that DB in liposomes was not toxic (Table 2). Furthermore, the cytotoxicity of CPT-loaded liposomes and CPT solution in DMSO was examined. IC_{50} of CPT solution, DB-L and HSA-DB-L showed 0.077, 0.048 and 0.042 μg CPT/mL. Despite of the existence of PEG2000 in liposomes, IC_{50} values of DB-L and HSA-DB-L were lower than that of CPT solution. The CPT lactone ring opened at about 20 min in medium, resulting in biological inactivity [6]. Incorporation of CPT in liposomes could maintain active lactone form even in the presence of serum, indicating that liposome formulations could keep the antitumor effect of CPT.

About Control-L, addition of PEG2000 to the liposomes increased incorporated efficiency of CPT from 30% to 75% (data not shown). The particle size and incorporation efficiency were not significantly different among all the CPT liposome formulations, and were about 150 nm and 80%, respectively.

Fig. 2. SDS-PAGE of HSA associated on the liposomes. Lane 1: HSA-DB-L (HSPC/Ch/OA/DB/PEG2000+HSA), Lane 2: HSA-DB-L without PEG2000 (HSPC/Ch/OA/DB+HSA).

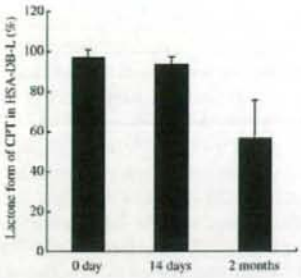

Fig. 3. Storage stability of lactone form of CPT incorporated in HSA-DB-L at room temperature. Each value represents the mean ± SD. ($n=3$).

when the liposomes were prepared at a feeding ratio of 1/30 (w/w) CPT/total lipid (Table 1). The effect of PEG on the association of HSA was evaluated using HSA-DB-L with or without PEG2000. The adsorbed HSA amounts on HSA-DB-L (HSPC/Ch/OA/DB/PEG2000+HSA) and HSA-DB-L without PEG2000 (HSPC/Ch/OA/DB+HSA) was 58.7±5.3 and 73.3±6.5 mg HSA/g HSPC, respectively. The presence of PEG reduced the association of HSA on the surface of DB-L compared with DB-L without PEG2000. This finding was also confirmed by SDS-PAGE as shown in Fig. 2. HSA-DB-L was successfully modified with HSA by incubation.

Moreover, analysis of HSA-DB-L, i.e., DB-L coated with HSA, demonstrated that neither the particle size nor the incorporation efficiency was changed by incubation of the liposomes with HSA. The surface potentials of DB-L and HSA-DB-L were −23.1±2.0 mV and −26.3±5.4 mV, respectively.

Drug release profiles of Control-L and DB-L showed that there was approximately 30% drug release from CPT liposomes into PBS over 72 h (data not shown), suggesting the CPT remained associated with the liposomes during the course of the study. This finding also suggests that CPT liposomes would be stable in dilute conditions.

3.2. In vivo circulation stability of CPT liposomes

To determine whether CPT liposomes were stable and long circulating, the plasma concentration of CPT liposomes was evaluated 4 h after mice were injected intravenously (Table 1). DB-L, which contained DB in addition to the formulation of Control-L, showed a significantly (about 3-fold) higher level CPT in the plasma compared to Control-L ($P<0.05$). This suggests that the addition of DB in the liposome bilayer increased the stability of CPT-incorporating liposomes in the blood. However, changing the PEG length from 2000 to 5000 (DB-L5000) or the addition of a 2-fold larger amount of DB in DB-L (2DB-L) failed to increase the CPT plasma concentration, although both formulations showed similar particle size and incorporation efficiency as DB-L. The result suggests that the level of incorporation of DB influenced on the distribution of CPT in liposomes.

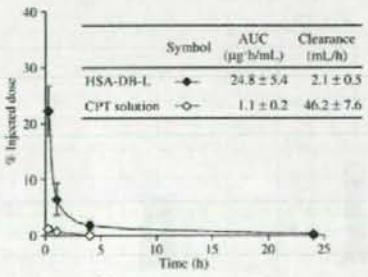

Fig. 4. Plasma concentration–time curves of the HSA-DB-L and CPT solution following i.v. injection at a dose of 2.5 mg CPT/kg in ddY mice. Each value represents the mean ± SD. ($n=3$).

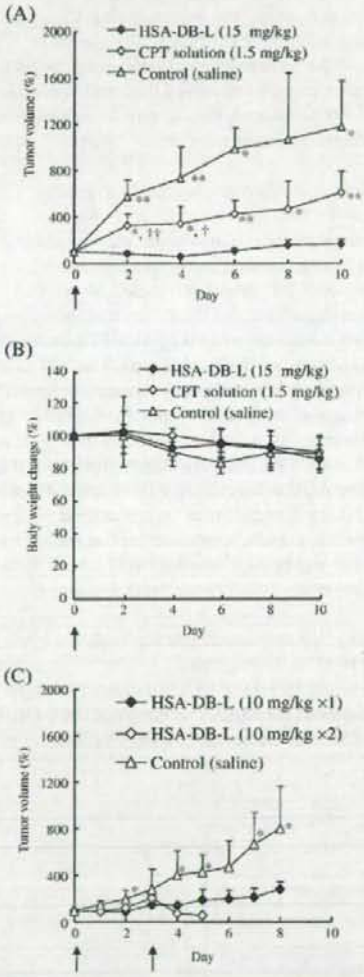

Fig. 5. In vivo antitumor activity in mice bearing C26 tumors. (A, B) Tumor volume and body weight change after a single injection of 15 mg/kg CPT in HSA-DB-L or 1.5 mg/kg CPT solution. (C) Single or repeated injection of 10 mg/kg CPT in HSA-DB-L. Arrows indicate the day of drug injections. Tumor volumes are plotted as ratios to their volume prior to the first drug injection. Each value represents the mean ± S.D. ($n=4$) *$P<0.05$, **$P<0.01$ compared with HSA-DB-L, †$P<0.05$, ††$P<0.01$ compared with control.

It has been reported that pre-coating polystyrene particles with HSA enhanced their stability in blood [23]. To increase the circulation stability of DB-L, therefore, the surface of DB-L was coated with HSA (HSA-DB-L). HSA-DB-L showed significantly (about 2.5-fold) higher CPT plasma concentration than DB-L ($P<0.01$).

3.3. Storage stability of CPT liposomes

Generally, the carboxylate form of CPT binds with HSA and is changed to the pharmacologically ineffective carboxylate form [5]. Therefore, the storage stability of HSA-DB-L at room temperature was examined by measuring the amount of CPT lactone form remaining by HPLC. As shown in Fig. 3, more than 95% of the lactone form of CPT in HSA-DB-L remained 14 days after preparation ($P>0.05$), and more than 50% at 2 months compared with that on day 0 without change of the size/polydispersity index over time.

3.4. Plasma concentration–time profiles in mice

As shown above, CPT liposomes that were stable in the blood circulation and in storage were obtained using an appropriate formulation of CPT liposomes coated with HSA. Next, the plasma pharmacokinetics of the HSA-DB-L was compared with these of CPT solution in mice (Fig. 4). CPT solution disappeared very quickly from the blood circulation. The CPT in HSA-DB-L was clearly more stable in the blood circulation than CPT solution. The percentage of the injected dose of HSA-DB-L remaining in plasma 15 min, 1, and 4 h after injection was significantly (19.5-, 10.9-, and 44.5-fold, respectively) higher than that of CPT solution. The AUC values of HSA-DB-L and CPT solution were 24.8 and 1.1 μg·h/mL, respectively, and their clearance values were 2.1 and 46.2 mL/h, respectively. Thus, HSA-DB-L showed about 22-fold higher AUC and a 22-fold lower clearance values than CPT solution.

3.5. Efficacy of single or repeated administration of CPT liposomes in C26-bearing mice

The efficacy of a single i.v. injection of HSA-DB-L at a dose of 15 mg CPT/kg against the growth of C26 in tumor-bearing mice was evaluated by monitoring tumor growth (Fig. 5(A)). The dose of CPT liposomes was decided from data that CPT-loaded polymeric micelles showed the maximum dose was 30 mg/kg after a single i.v. administration to mice [12]. HSA-DB-L showed much higher antitumor activity than CPT solution or the saline control. Mice treated with CPT solution showed a significantly smaller tumor volume than control mice. The relative tumor volume (%) in HSA-DB-L-treated mice was significantly lower than that in mice treated with the saline control or CPT solution with treated/control (T/C) volume of 16.4% at Day 8. The mice treated with HSA-DB-L as a single i.v. injection at a dose of 15 mg CPT/kg did not show any significant body weight loss during the observation period (Fig. 5(B)). The dose of CPT solution used (1.5 mg CPT/kg) was 10-fold lower than that of HSA-DB-L. The dose could not be increased, because in preliminary experiments a higher dose (2.5 mg/kg) often resulted in death after i.v. injection. Thus, the antitumor treatment with HSA-DB-L would have yielded a higher plasma concentration of CPT, and this may have accounted for the larger antitumor effect than that of CPT solution.

In order to increase the efficacy of the treatment using HSA-DB-L, the administration schedule was changed to repeated injection using a decreased dose (10 mg/kg instead of 15 mg/kg) on Days 0 and 3 (Fig. 5(C)). A single injection of HSA-DB-L at a dose of 10 mg CPT/kg showed significant antitumor activity with T/C% of 34.6 at Day 8. Repeated injection of HSA-DB-L resulted in a body weight loss of approximately 20% on the third day after the second injection (data not shown), and within 2 more days, all of the treated mice died. This seemed to be related to CPT toxicity, because when empty HSA-DB-L (not containing CPT) was injected in mice on the same schedule as used in Fig. 5(C), no mice died (data not shown).

3.6. Biodistribution of CPT liposomes in tumor-bearing mice

Fig. 6(A) shows the amount of CPT in tissues of mice bearing C26 tumors, and Fig. 6(B) shows the percent of the dose of injected CPT in the blood 24 h after the injection of HSA-DB-L. Tumor tissue exposed to HSA-DB-L demonstrated significantly (9.6-fold) higher CPT accumulation than tumor tissue exposed to CPT solution ($P<0.05$). CPT accumulation of HSA-DB-L in liver and lung was decreased but that of kidneys was increased

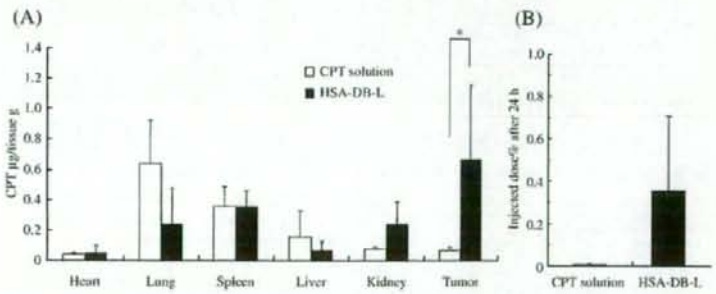

Fig. 6. Biodistribution of CPT 24 h after i.v. injection of HSA-DB-L or CPT solution (2.5 mg CPT/kg) into mice bearing C26. (A) Amount CPT per tissue weight. Each value represents the mean±S.D. ($n=3$) *: $P<0.05$ (B) % of injected dose of CPT in plasma. Each value represents the mean±S.E. ($n=3$).